May 2021

Mechanism Behind Grain Boundary Segregation and Mechanical Properties Enhancement of CoCrFeMnNi High Entropy Alloy Through Molecular Dynamics Simulation

Zibusiso Dhlamini
Clemson University, dhlaminz@gmail.com

MECHANISM BEHIND GRAIN BOUNDARY SEGREGATION AND MECHANICAL PROPERTIES ENHANCEMENT OF CoCrFeMnNi HIGH ENTROPY ALLOY THROUGH MOLECULAR DYNAMICS SIMULATION

A Thesis
Presented to
the Graduate School of
Clemson University

In Partial Fulfilment
of the Requirements for the Degree
Master of Science
Mechanical Engineering

---

by
Zibusiso Dhlamini
May 2021

Accepted by:
Dr. Huijuan Zhao, Committee Chair
Dr. Fadi Abdeljawad
Dr. Garrett J. Pataky

ABSTRACT

Grain boundaries play an important role in mechanical properties of metallic alloys. The element segregation of metallic alloys at grain boundary can impact the strength of the alloy by changing the underlying deformation mechanism. Current studies of grain boundary segregation are mainly focused on binary alloys. With the newly developed high entropy alloys, it is necessary to investigate the role of grain boundary segregation on the mechanical properties of the high entropy alloys. Therefore, we conduct an atomistic study of elemental distribution on the grain boundary of the bicrystal CoCrFeMnNi high entropy alloy and investigate the relation between grain boundary segregation and the mechanical strength of the material. Hybrid Monte Carlo (MC) and Molecular Dynamics (MD) simulations are performed to obtain the equilibrium state of elemental distribution within the grain and on the grain boundary of the bicrystal model of CoCrFeMnNi high entropy alloy. The grain boundary is defined as $\sum 5$ (3 1 0) [0 0 1] $\theta = 36.9^{o}$. It is found that Cr has a propensity to segregate to the boundary. With the consideration of various dopant elements at the grain boundary of this bi-crystal model, MD/MC simulations are performed to study the role of selected dopant on the grain boundary to the mechanical strength of the material under the uniaxial loading conditions. The results reveal that the presence of Cr on the grain boundary has an embrittling effect to the alloy while Ni leads to an increase in yield and ultimate strength. The embrittling effect is due to the low stress requirement to nucleate dislocations in a Cr dopped grain boundary. Conversely, a higher dislocation density was observed during the deformation of bicrystal with the Ni dopped grain

boundary. Such dislocations could traverse between grains without pinning leading to an increase in strength. Under compression, however, there was no significant difference in strength and elastic modulus with respect to different dopants on the grain boundary. This work leads to further study on the tailoring of high entropy alloys' mechanical properties through grain boundary manipulations.

ACKNOWLEDGEMENTS

I would like to first thank my advisor Dr. Huijuan Zhao for her support, patience, and guidance throughout the process of conducting my research. I have been very fortunate to be part of the CMML research group for the past two years and have learned a lot about computational mechanics and materials. I was worried coming in with limited simulation experience, but it was never an issue thanks to the faith my advisor had in me and the immense knowledge she has. I would like to thank Dr. Fadi Abdeljawad for informative discussions on molecular dynamics simulations, and Dr. Garrett Pataky for introducing high entropy alloys to me and providing an experimental perspective to the project. I am grateful for the financial support provided by the Department of Mechanical Engineering and the excellent computing resources provided by CCIT at Clemson University. The professors and staff have been very knowledgeable and supportive. I would like to thank my groupmates Mahababur Rahman, Tristan Woods, and Dr. Qian Mao for insightful discussions on simulations and software issues. Finally, I would like to thank my family for the emotional support and standing by me throughout the course of my education.

Table of Contents

LIST OF FIGURES

LIST OF TABLES

CHAPTER 1. INTRODUCTION

1.1 Definition of High Entropy Alloys

High entropy alloys (HEAs) or multi-principal element alloys (MPEAs) are a class of non-conventional metal alloys where the alloys are lacking a base element, commonly with equimolar elemental fractions [1][2][3][4][5][6][7]. Since traditional alloys consist of one or two base elements with small amounts of other alloying elements, the resulting alloys usually retain the properties of the element with the largest concentration. For example, the aluminum alloys contain up to 99% weight percentage of aluminum element and a small percentage of at least one other element. While maintaining their high strength to weight ratio, the aluminum alloys have significantly improved material properties such as high strength, corrosion resistance, electrical conductivity, and flexible workability [8]. On the contrary, HEAs are originally defined as alloys composed of 5 or more elements at chemical compositions between 5% and 35% [1]. Yeh [1] hypothesized that the high configurational entropy of a multi-element system would lower the Gibbs free energy of the system and lead to a stable solid solution. The Gibbs free energy G quantifies the amount of work performed by a thermodynamic system at constant pressure and temperature. Its variation is calculated as

$$\Delta G=\Delta H-T\Delta S \tag{1.01}$$

where ΔG is the change in Gibbs energy, ΔH is the change in enthalpy, T is temperature and ΔS is the change in entropy. Therefore, a negative ΔG can be observed with a positive ΔH if the entropy change ΔS is large enough at the selected temperature T. Entropy can be

further decomposed into configurational, electronic, vibration, and magnetic entropy [9]. The configurational entropy ΔS_{conf} contributes to the entropy and is given by

$$\Delta S_{\text{conf}} = k_{\text{B}} \ln \omega = -nR \sum_{i=1}^{j} x_i \ln (x_i) \tag{1.02}$$

where ω is the number of ways that atoms can be arranged, $k_{\text{B}}=R/n$ is the Boltzmann's constant, n is the number of moles in the system, R=8.31JK^{-1}mol^{-1} is the gas constant, and x_i is the fractional composition of element i in a system containing total j element types. A key assumption is that atoms were randomly distributed to maximize entropy. Cantor [2] later showed that the increase in entropy of multicomponent systems was not sufficient to justify the formation of solid solutions. It is experimentally proved that an equiatomic alloy containing 20 elements results in a brittle multi-phase microstructure despite having a larger configuration entropy than a 5-element solid solution alloy [2]. This indicates that entropy alone is not enough to explain the formation of solid solution HEAs and enthalpy should also be considered. Hence names such as multiple principal elements and complex concentrated alloys have been adopted [10].

1.2 Characterization of HEAs

As a product of the cocktail effect [11] of identifying alloy candidates to take advantages of their individual characteristics, HEAs exhibit high strength and hardness [12], excellent wear [13] and corrosion resistance [14][15]. For example, light elements such as aluminum can reduce the density of HEAs [16]. A combination of various size atoms can lead to local lattice distortions which introduce high energy barriers to prevent dislocation motion. Therefore, the strength of the HEAs can be greatly enhanced [17].

Miracle and Senkov [18] identified several major families of HEAs. The first group and most widely studied is made from 3d transition metals: Al, Co, Cr, Cu, Fe, Mn, Ni, Ti, and V. This group includes the pure 3d transition metals combination CoCrFeMnNi, CoFeMnNi, CoCrFeNi and CoCrFeNi, and the combination of transition metals and large atom elements: $Al_xCoCrFeNi$, $Al_xCoCrCuFeNi$, $Al_xCoCrFeMnNi$, $AlCoCrCuFeNiTi_x$, and $AlCoCrFeNiV_x$. Mechanical properties of 3d transition metal HEAs are similar to austenitic steels and nickel alloys. 96% (331 out of 345) alloys in this group contain Fe, 29% contain Mn and 15% use V [18]. The addition of large radius atoms to pure 3d transition HEAs increases the yield strength by dislocation strengthening, twinning

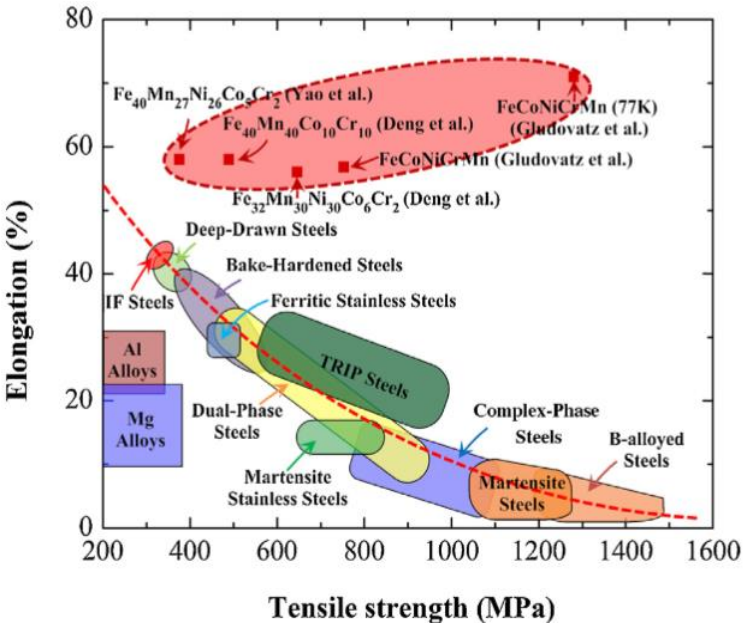

Figure 1. 1 Tensile strength versus ductility of $Fe_{40}Mn_{27}Ni_{26}Co_5Cr_2$, $Fe_{32}Mn_{30}Ni_{30}Co_6Cr$, FeCoNiCrMn and other traditional alloys[20]

strengthening, and precipitation strengthening [19]. Figure 1.1 presents the comparison of strength-elongation relation between HEA and traditional alloys. HEAs show the potential to solve the strength-ductility paradox of alloy development.

Combinations of refractory elements Cr, Hf, Mo, Nb, Ta, Ti, V, W, and Zr, with Al make up the second group. These were developed for their high strength at elevated temperatures which are critical for aircraft and aerospace applications. For example, NbMoTaW and VNbMoTaW developed by Senkov *et al.* have mechanical properties comparable to Ni-base superalloys, with compressive yield strengths that are insensitive to temperature above 600ºC to 1600ºC and only dropping by 30-40% from room temperature to 600ºC [21]. Shown in Figure 1.2, Cr containing refractory HEAs CrNbTiVZr and CrNbTiZr have higher specific yield strengths than Ni super-alloys (In718 and Haynes 230) under uniaxial compression at temperatures between 200ºC and 1400ºC [22]. Figure 1.3 also shows the resistance to thermo-softening of other refractory HEAs compared to

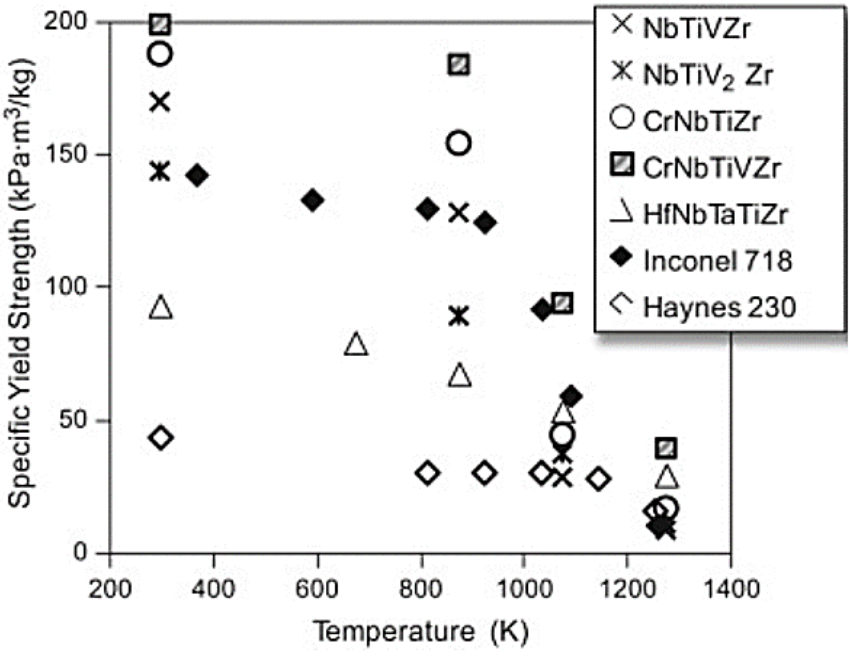

Figure 1. 2 Variation of specific yield strength with temperature for Cr based HEAs CrNbTiZr and CrNbTiVZ in comparison with other refractory HEAs, Inconel, and Haynes superalloys [22]

the superalloys that makes them candidates for power, aerospace, and chemical processing industries [20].

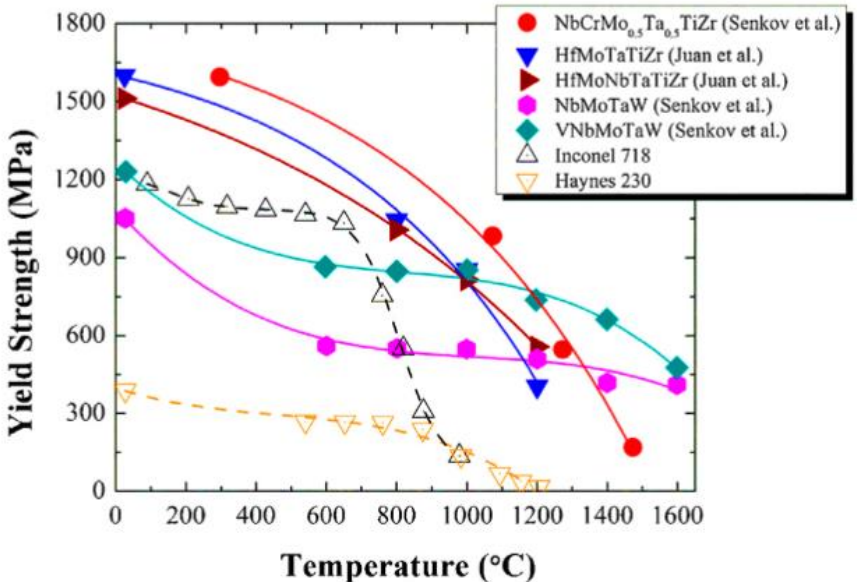

Figure 1. 3 Variation of yield strength with temperature of refractory HEAs, Inconel 718 and Haynes 230 [20].

The third family of low-density alloys are primarily developed as lightweight structural materials for aerospace applications. It consists of Al, Be, Li, Mg, Sc, Si, Sn, Ti and Zn, such as AlFeMgTiZn [23], AlLiMgZnSn, $AlLi_{0.5}MgZn0.5Sn_{0.2}$, $Al_{80}Li_5Mg_5Zn_5Sn_5$ [24]. These HEAs have low density (density less than 7g/cm^3) and high mechanical strength. Shao *et al.* used vacuum induction melting to fabricate the multiphase alloys $Al_{58.5}Mg_{31.5}Zn_{4.5}Cu_{4.5}Si_1$; $Al_{63}Mg_{27}Zn_{4.5}Cu_{4.5}Si_1$; $Al_{66.7}Mg_{23.7}Zn_{4.5}Cu_{4.5}Si_1$; $Al_{80}Mg_{14}Zn_{2.7}Cu_{2.7}Si_{0.6}$, $Al_{85}Mg_{10.5}Zn_{2.025}Cu_{2.025}Si_{0.45}$, and $Al_{90}Mg_7Zn_{1.35}Cu_{1.35}Si_{0.3}$ [25]. Under compressive loading at room temperature, these alloys had fracture strengths of 577, 677, 590, 498, 814, and 794 MPa, respectively. Their densities are between 2.64 to 2.71 g/cm^3. For comparison, the average density of titanium alloys is 4.5g/cm^3 [25]. Recently, Tseng *et al.* developed the lightweight HEA $Al_{20}Be_{20}Fe_{10}Si_{15}Ti_{35}$ with a density of 3.91 g

/cm^3 and hardness of 911 HV, which is higher than quartz, and fracture strength of 2976 MPa (calculated using the formula of HV ~ $3\sigma_f$) [6]. The HEA had better oxidation resistance than Ti-6Al-4V making it an excellent candidate for high temperature lightweight applications [6].

The fourth family is composed of at least four of the lanthanide (4f) elements Dy, Gd, Lu, Tb and Tm, with Y. These alloys show solid solutions with HCP structures. Motivated by scientific curiosity, scientists seek to discover single-phase, solid solution high entropy alloys (HEAs) with the HCP crystal structure in this family. DyGdLuTbY and DyGdLuTbTm are the only alloys found as present.

1.3 Mechanical Properties of HEAs

Figure 1.4 shows the fracture toughness as a function of yield strength for different types of materials. The toughness of HEAs exceeds that of most pure metals and alloys, and their yield strength is comparable to that of low alloy steels.

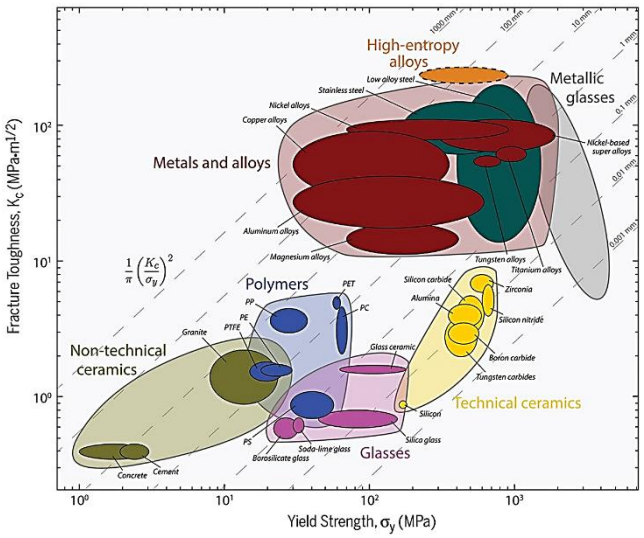

Figure 1. 4 Ashby map of fracture toughness versus yield strength relations [20].

Properties of HEAs available in the literature are summarized in Table 1.1 [26]. The group number of each HEA is indicated with color code as green in group 1, yellow in group 2 and blue in group 3. The testing type (T for tension and C for compression) and testing temperature of test are listed. It shows most HEAs in group 1 and 2 have FCC/BCC lattice structure. The first two rows present that processing of cold drawn can increase the ultimate strength of CoCrFeNi HEA from 413 MPa to 1224 MPa.

Table 1.1 Mechanical properties of HEAs from experimental tests in literatures.

HEA	Phase	Temp (K)	Test	Processing Route	σ_y (MPa)	σ_{max} (MPa)	E (GPa)
CoCrFeNi [27]	FCC	300	T	as cast	148	413	225
CoCrFeNi [28]	FCC	223	T	cold drawn	1224	1224	-
AlCoCrFeNi [29]	BCC	300	C	as cast	1138	-	194
$Al_{0.20}$CoCrFeMnNi [30]	FCC	300	T	cold rolled, annealed	220	-	214
$Al_{0.25}$CoCrFeMnNi [31]	FCC	300	T	cold rolled, annealed	139	805	-
$Al_{0.56}$CoCrFeMnNi [30]	FCC BCC	300	T	as cast	526	-	204
CoCrMnNi [32]	FCC	300	T	annealed, quenched, cold rolled	282	694	222
CoCrFeMnNi [33]	FCC	300	T	cold rolled, annealed	888	984	-
CrHfNbTiZr [34]	BCC Im*	300	C	annealed	1375	-	112
HfMoNbZrTi [35]	BCC	300	C	annealed	1803	1719	139
HfNbTaTiZr [36]	BCC	300	T	cold forged	1438	1495	92
AlLiMgSnZn [37]	FCC HCP Im	300	C	-	600	615	-
MgCaAlLiCu [38]	Tetra	300	C	as cast	-	910	-

*Im: Intermetallic

1.4 Limitations of HEAs

Even though the HEAs present enhanced mechanical properties, there are still challenges hindering the adoption of HEAs in real world applications. The processing techniques are expensive. The promising refractory HEAs are dense and brittle. Senkov's NbMoTaW refractory alloy only had a fracture strain of 2.6% at room temperature despite its high yield and ultimate strength of 1058MPa and 1211MPa respectively under compression [21]. VNbMoTaW had a low fracture strain of 1.7% but a yield strength of 1246MPa and ultimate strength of 1270MPa at room temperature [21]. Due to the large number of possible element combinations that can result in a HEA, it is challenging to accurately predict the solid phase formation of HEA due to its sensitivity to the processing routes and conditions [39]. For example, the commonly studied AlCoCrFeNi HEA has a single BCC phase and a room temperature hardness of 484Hv under a 5kg load, with load time of 15s, and load rate of 50μm/s. Yet after homogenization at 1100^{o} for 24hours and water quenched, it has a duplex FCC-BCC structure with a lower hardness of 433Hv under the same loading conditions [39]. Therefore, it is difficult to accurately predict the material property in the experimental screening process of HEA design.

1.5 Numerical Simulations of HEAs

Since it is difficult to precisely design and fabricate the HEAs experimentally due to its composition complexity [40] and phase stability, computational modeling and simulations provide a more practical pathway to alloy design and to understand the material properties. Numerical simulations on HEAs have been carried out using molecular dynamics (MD) simulations, hybrid Monte Carlo (MC)/MD simulations, and first-

principles density functional theory (DFT) calculations. Huang *et al* investigated the scratch resistance of AlCoCrFeNi using MD simulations carried out by the Forcite module in Materials Studio® (Accelrys Software Inc.) [41]. Their study employed a condensed-phase optimized ab-initio force field (COMPASS). The AlCoCrFeNi HEA is constructed by randomly positioning atoms at face-centered-cubic (FCC) crystal structure sites, equilibrating above the melting temperature (2200K) and rapidly quenching to room temperature [41]. Using an EAM (embedded atom method) potential developed by Zhou *et al.* [42], Meraj *et al.* investigated the deformation mechanism in NiWCuFeMo under alternating cycles of uniaxial compression and tension. The study finds that the dominant deformation mechanism is twinning for tensile forward loading while atomic diffusion is the dominant deformation behavior in compressive reverse loading [43]. Rao *et al.* used the same potential to study the structure and glide motion of dislocations in a randomly distributed model-BCC $Co_{16.67}Fe_{36.67}Ni_{16.67}Ti_{30}$ alloy. They found a weaker temperature dependence of critical glide stress with temperature of this alloy compared to pure BCC Fe [44]. Combining MC with MD simulation allows to efficiently determine chemical order of the HEAs compared to conventional MD due to the absence of energy barrier-related limitations [45]. Widnom *et al.* utilized ab initio MD and MC simulations in VASP to determine the pair ordering in MoNbTaW at different temperatures [45]. Strong bindings are revealed between Ta-W, Ta-Mo, Nb-W, and Nb-Mo [45]. Patriarca *et al.* also used first principles DFT calculation to determine the lattice constant and critical resolved shear stress (CRSS) in CoCrFeMnNi. They predict an equilibrium lattice constant $a_0 = 3.59$ Å which is in close agreement with the lattice constant $a_0 = 3.585$ Å determined

using X-ray diffraction. The CRSS value is 178 MPa, matching with experimental observations (τ_{77K} = 175 MPa) as well [91].

DFT calculations of HEAs is accurate but expensive, limited by the system size and complicated HEAs lattice structures and atom positions. MD/MC simulations of HEAs are flexible to handle large volume of atoms and computationally less expensive compared to DFT calculations. However, the accuracy of MD/MC simulations depends on the availability of well benchmarked empirical potentials.

1.6 Grain Engineering Strategies

Grain refinement is an attractive strengthening mechanism for increasing strength of alloys. Hall [47] and Petch [48] observed that the yield stress of iron and steel increases with decreasing grain size for grain sizes between 1-100 μm, leading to the famous Hall-Petch relationship:

$$\sigma = \sigma_o + Kd^{-1/2} \tag{1.03}$$

where σ_o is the dislocation retarding stress, d is the grain size, and K is a material constant [49]. This relationship extends to nanocrystalline materials, although the slope K becomes less steep and even negative at a critical grain size [50]. Fine grains can be achieved by repeated heating and cooling cycles, severe plastic deformation, and a combination of both thermal treatment and plastic deformation. Hodgson *et al.* created a refined ferrite microstructure with a large fraction of average grain sizes of 1μm using severe plastic deformation of austenitic steel [51]. Equal Channel Angular Extrusion (ECAE) is a metal working process for producing ultrafine grains by plastic straining while keeping the cross-

sectional area of the workpiece at low temperatures. Large shear strains are applied by pushing the workpiece through an angled channel die with the same cross- sectional shape. Fang *et al.* studied the effects of ECAE passes on the microstructure, tensile strength, and ductility of Al–0.63 wt.% Cu and Al–3.9 wt.% Cu alloys. They discovered that the grains of the two alloys are refined to submicron level after four passes. The tensile strength of Al–0.63% Cu increases from 83 to 239 MPa while that of Al–3.9% Cu increases from 207 to 290 MPa [52]. Grain refinement can also be achieved at the fabrication stage of the material. Ball milling is a common method to obtain nanosized particles through mechanical attrition [53]. Powders can then be consolidated using sintering techniques to form nanocrystalline alloys [54]. Electrodeposition also results grain sizes in the nanocrysalline range when electrodeposition variables are tailored to inhibit the growth of existing grains but promote new grain nucleation [55]. This method results in materials with low porosity and hence there is no need for further consolidation processing [55]. Other techniques to synthesize ultra-fine-grained materials include external fields during crystallization [56], and inert gas condensation [57].

In addition to grain refinement, grain interfaces can also influence mechanical properties. Grain boundary (GB) solute segregation can stabilize grain boundaries and detain grain boundary sliding and migration [58]. In MD simulations, a commonly adopted method of introducing dopants at grain boundaries is to select solvent atoms around the grain boundary and randomly replace them with solute atoms to achieve the desired boundary concentration. Liu *et al.* [59] used this technique to investigate the effects of different concentrations of Ni impurities on shear induced dislocation

nucleation in the ∑9 grain boundaries in Cu. Such a method, however, does not result in energetically stable configurations as it is does not consider the potential energy of the system. Borovikov [60] extended this method to study the effects of either oversized (Ag in Cu) or undersized (Cu in Ag) grain boundary dopants on the yield strength of a Σ11(332) [110] bicrystal. Dopant atoms were randomly introduced to a large region extending 3nm normal to the boundary. Monte Carlo atom swaps were conducted within the region such that the overall concentration in the bicrystal was conserved. An MD study done by Babicheva *et al.* [58] showed that the tensile strength of nanocrystalline Al–10.2 at.%Co with Co distributed along the grain boundaries was higher than that of pure nanocrystalline Al. The grain boundary dopped nanocrystalline Al–10.2 at.%Co also had a higher tensile strength compared to the same alloy with randomly dispersed Co atoms. Zhou *et al.* confirmed grain boundary type dependent segregation of Cr in nanocrystalline Fe(Cr) both experimentally and numerically through molecular dynamics (MD) and Monte Carlo (MC) simulations [61].

From thermodynamics, segregation is driven by the objective to reduce the free energy at the grain boundary [62]. Segregation of large radius atoms from the bulk into grain boundaries results in the decrease in elastic strain energy. Excess volume is the main driver behind enhanced diffusion of impurities along GBs [63]. Both interfacial energy and excess volume depend on grain boundary type (tilt, twist) and geometry (misorientation angle). There is a direct correlation between the grain boundary energy and excess volume [64]. To characterize a grain boundary experimentally, the GB misorientation and GB plane are needed to be determined. GB Misorientation can be determined from two-

dimensional Electron Backscatter Diffraction (EBSD) but additional sectioning is required to find the normal direction of the GB plane. Site specific Atom Probe Tomography (APT) is commonly used to quantify the degree of segregation at the interfaces [65] [66]. Comparing to the experimental characterizations of GBs, atomistic simulations are more practical to investigate large number of GB types and various GB segregations.

Therefore, we will adopt atomistic simulations to investigate the role of GB and GB segregation to the strength and toughness of the HEA alloys.

1.7 Literature Review and Research Objectives

Substantial work has been done on further improving the strength of the Canter HEA (CoCrFeMnNi) by grain refinement through severe plastic deformation and annealing processes [67][68]. This alloy exhibits an increase in yield strength with decreasing temperatures and high strength and ductility at cryogenic temperatures [19]. Such pronounced work hardening is attributed to the change from slip mediated deformation to twinning [19]. Additionally, it has good fracture toughness and crack growth resistance comparable to austenitic stainless steels [76]. Introducing interstitial elements can increase the strength of Canter HEAs. Luo *et al.* investigated the effects of hydrogen on the tensile properties of CoCrFeMnNi[69]. Their results showed that hydrogen alloying increased both the strength and ductility of the HEA by enhancing the twin formation during deformation. Li studied the effects of low concentrations of carbon, microstructure, and compositional homogeneity on the mechanical properties of Canter CoCrFeMnNi[70]. He found that the yield strength increases when carbon content is increased from 0 to 0.8 at. %. The ultimate strength of the grain refined and

homogenized HEA nearly doubles. This increase in strength can be attributed to the retardation of post annealing recrystallization by the interstitial carbon [70]. Interstitial atoms can also lead to the formation of second phases. These can add to the strengthening effect as is the case with N_2 [71]. Alloying elements such as Al [72], V [73], Nb [74], and Ti [74] have also been added to the HEA to create second phases (BCC, HCP, Sigma or Laves) with higher yield strength [75]. Knowledge of the grain boundary elemental composition helps researchers understand the mechanical and chemical behavior observed in the HEA. Moreover, GB segregation leads to the depletion of the segregating element in the region immediately outside the GB, and an increase in its concentration at the interface. Depending on the element, this could promote or reduce intergranular corrosion and fracture. Secondary phases may result from GB segregation leading to intergranular fracture. Ni depleted intergranular borides containing Cr and Mo have been experimentally observed in N18 superalloy [77]. These borides can cause grain boundary induced liquidation leading to hot cracking under uniaxial tension [78]. Cr segregation in metal alloys has been a subject of great interest because of its potential effects on material properties. Li-dong *et. al* reported a high Cr concentration of in martensitic/ferritic grain boundaries after heat treatment [79]. Studies of Charpy test fracture surfaces of Cr martensitic steel with 10.5 wt% of Cr samples indicated a high Cr concentration of 20% [80]. Further analysis showed that cracks followed Cr enriched regions. Cr segregation was also observed in a FeCrNi alloy using EBSD and EDS mapping at multiple grain boundaries with different misorientation angles [81]. Molecular

Dynamics simulations of selective laser melted FeCrNi show the formation of Cr rich nanoclusters[82].

Despite the growing interest in the enhancement of the properties of HEAs, grain boundary segregation in polycrystalline and nanocrystalline CoCrFeMnNi has not been thoroughly explored. The objective of this study is to understand the grain boundary and surface segregation behavior in CoCrFeMnNi by quantifying the local chemistry at these sites. In this study, MC and MD simulation techniques will be used to investigate equilibrium grain boundary segregation at a symmetric tilt grain boundary in a bi-crystal of Canter CoCrFeMnNi HEA at room temperature. Surface segregation will then be analyzed by introducing free surfaces to the bicrystal to determine preferred segregation when both surfaces and GB are present. Chemical ordering inside the bulk HEA is also studied using radial distribution function plots to determine nanoclustering behavior. Finally, we study the effects of different dopants at the grain boundary on the mechanical properties of the bi-crystal CoCrFeMnNi by subjecting the HEA to uniaxial tension and compression loading. From a grain boundary engineering perspective, the goal is to elucidate the relation between grain boundary segregation and mechanical property enhancement of the HEA. The goal is to tailor mechanical properties of the Canter HEA through grain boundary segregation.

As following, Chapter 2 reviews grain boundary definition, classification, and their role to the material property. The background of atomistic modeling method adopted in this study is also introduced. Chapter 3 presents the results and discussion of grain boundary segregation and short-range ordering in the HEA. In Chapter 4, the effects of

selective doping at the grain boundary to the tensile and compressive strength of the bi-crystal Canter alloy are investigated. Conclusions and future work are listed in Chapter 5.

CHAPTER 2. THEORIES AND METHODS

2.1 Introduction to Grain Boundaries

2.1.1 Definition of Grain Boundaries

Grain boundaries (GB) are the interfaces between grains in polycrystalline materials formed during the crystallization process. Classified as planar defects, they are regions of atomic disorder where atoms are not in perfect crystalline positions. This results in excess free energy per unit area with respect to a reference perfect crystal, and a thermodynamic force to reduce the fraction of grain boundaries in a polycrystal. In FCC alloys, the average GB thickness is 0.5nm, defined as the width of the transition region at the junction of two grains where atoms are not perfectly aligned with either grain. For BCC alloys, the average GB thickness is larger than 1.0nm [83] [84].

2.1.2 Classification of Grain Boundaries

Based on geometry, grain boundaries can be classified into tilt, twist and mixed boundaries. To form a tilt GB, two grains are rotated about an axis that lays on the GB plane by a misorientation angle θ, resulting in an array of edge dislocations with the Burgers vector $\boldsymbol{b}$ perpendicular to the GB plane. To form a twist GB, two grains are rotated about an axis perpendicular to the GB plane and resulting in a network of screw dislocations. Mixed GB is a combination of the two. Figure 2.1 shows the schematic of the tilt GB and twist GB. Small misorientation angles ($< 15^{o}$) result in low angle GBs, which allow dislocations to slip between grains easily. Large misorientation angle ($\theta > 15^{o}$) result in high angle GBs, bringing in large atomic mismatch and high GB energy. A grain boundary can be fully defined by the orientation of the constituent crystals with respect to

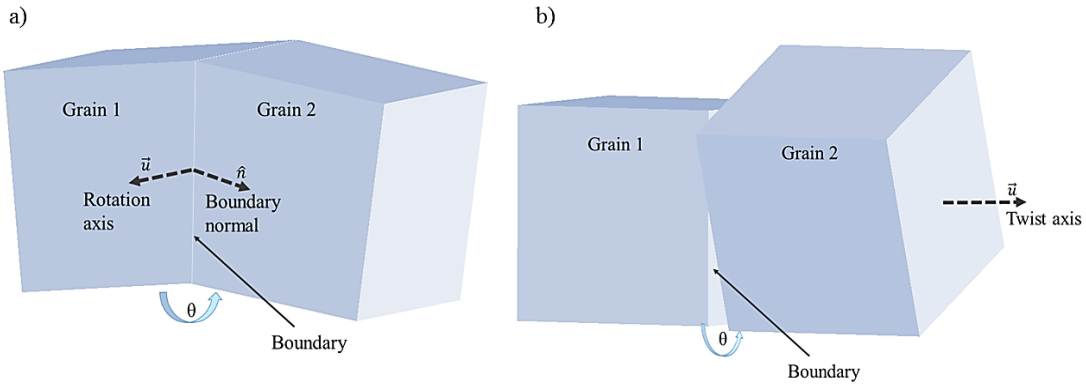

Figure 2. 1 Geometries of a) a tilt and b) a twist grain boundary

each other, and the orientation of the boundary plane with respect to one of the crystals. For example, *(hkl)* <*uvw*> *θ* denotes a grain boundary in which the GB plane's normal direction is *(hkl),* and the two grains have a misorientation angle *θ* about axis <*uvw*>. Defined by Frank's formula, the dislocation spacing *D* is related to the misorientation angle *θ* and the magnitude of the Burgers vector ***b***, shown as

$$D = \frac{b}{\sin(\theta)} \tag{2.01}$$

2.1.2 Coincidence Site Lattice (CSL) Classification

The Coincidence Site Lattice (CSL) classification is a method to recognize a special GB with desirable properties such as low energy, better corrosion resistance, and high fracture resistance. CSL is defined as the reciprocal density of coincidence sites. It is recognized that GBs have low interfacial energy at the misorientations corresponding to low values of the reciprocal of CSL density (Σ). For two interpenetrating crystals rotated about a common axis, CSL density (Σ) is defined as

$$\Sigma = \frac{\text{Volume of coincidence unit cell}}{\text{Volume of primitive unit cell}}. \tag{2.02}$$

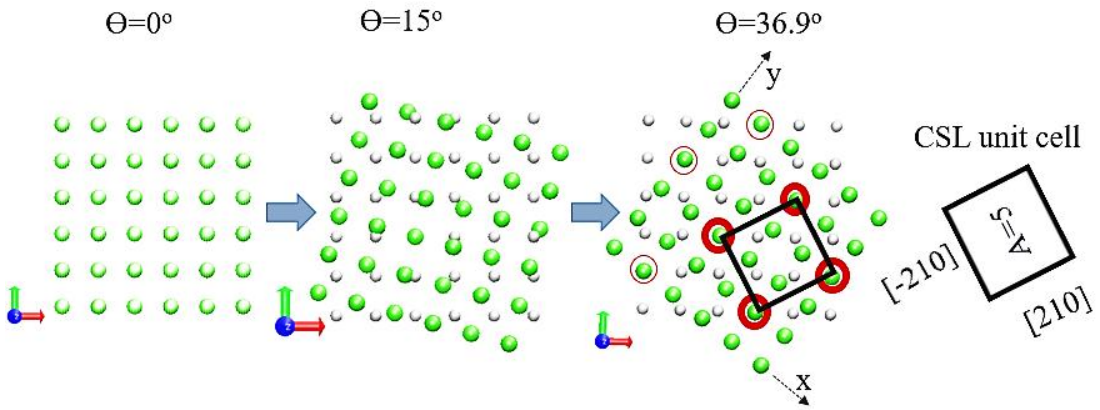

Figure 2. 3 Procedure for determining the Σ value of a CSL boundary. Coincidence sites are marked with red circles

Figure 2.2 shows how the Σ value is calculated for a Σ5 GB corresponding to a misorientation angle of 36.9° using two overlaid crystals. The black square represents the unit cell of coincident lattice sites. Using a coordinate system based on the floating crystal made up of the green atoms, the area of this unit cell in lattice constant units is 5. Since the area of the primitive unit cell is 1, the rotation angle corresponds to a Σ=5/1 boundary.

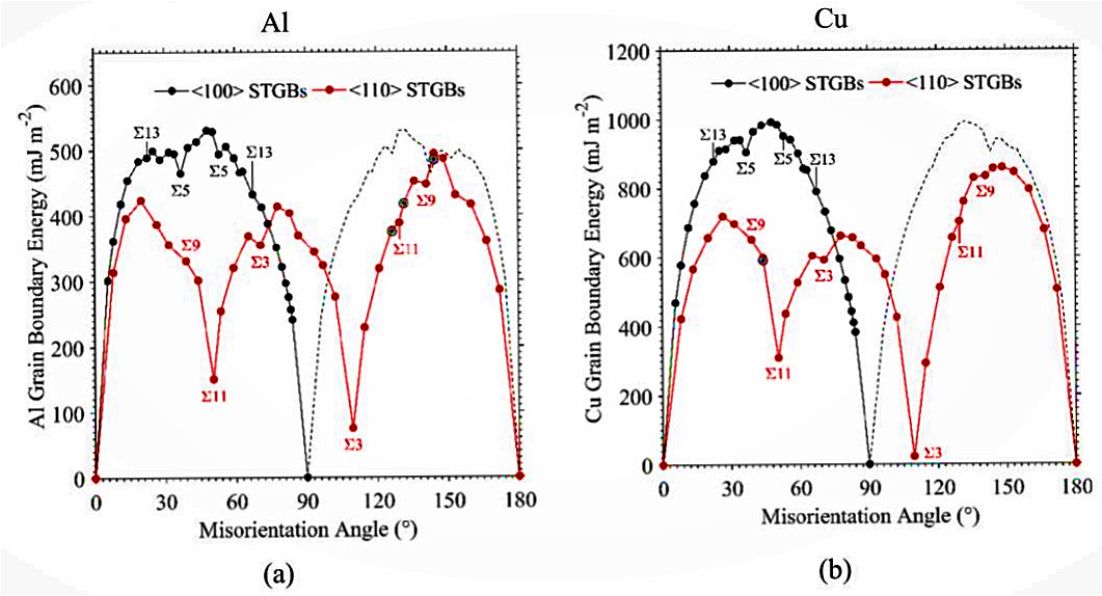

Figure 2. 2 GB energy variation with respect to misorientation angle in <100> and <110> tilt boundaries [85]

The CSL concept is purely a geometric simplification of boundaries. It does not consider the atom vibration at its site. The CSL density Σ is closely related with the GB energy. Non-CSL grain boundaries have higher atomic distortions and thus high energy. Tschopp *et al.* conducted molecular dynamics studies to quantify the misorientation dependence of GB in symmetric and asymmetric boundaries in Cu and Al with rotation axis <100> and <110> [85]. As seen in Figure 2.3, cusps corresponding to Σ3 and Σ11 GBs are identified in the <110> boundaries in both materials. For the <100> boundaries, cusps corresponding to Σ5 are identified.

2.2 Molecular Dynamics Simulations

Molecular dynamics is a computer simulation technique used to model the dynamic motion of atoms and molecules by solving the classical mechanics Newton's 2nd equations. Statistically, thermodynamic properties of a system can thus be obtained and interpreted based on the observed trajectories of the atoms and molecules at the atomistic scale.

2.2.1 Classical Mechanics

Defined by Newton's 2nd equation, the force on an atom is given by:

$$\mathbf{F}_i = m_i \mathbf{a}_i \tag{2.03}$$

where $\mathbf{F}_i$, m_i and $\mathbf{a}_i$ are the force vector, the mass and the acceleration vector of the atom i respectively. At a given time t, the force vector $\mathbf{F}_i$ is defined as the gradient of the potential energy U_i:

$$\mathbf{F}_i = -\nabla U_i(\mathbf{r}_i) \tag{2.04}$$

Where $U_i(\mathbf{r}_i)$ is the potential energy of the atom i at position $\mathbf{r}_i$, describing the interaction of the atom i and its surrounding atoms. The acceleration vector is defined as

$$\mathbf{a}_i = \frac{\mathrm{d}^2\mathbf{r}_i}{\mathrm{d}t^2} \tag{2.05}$$

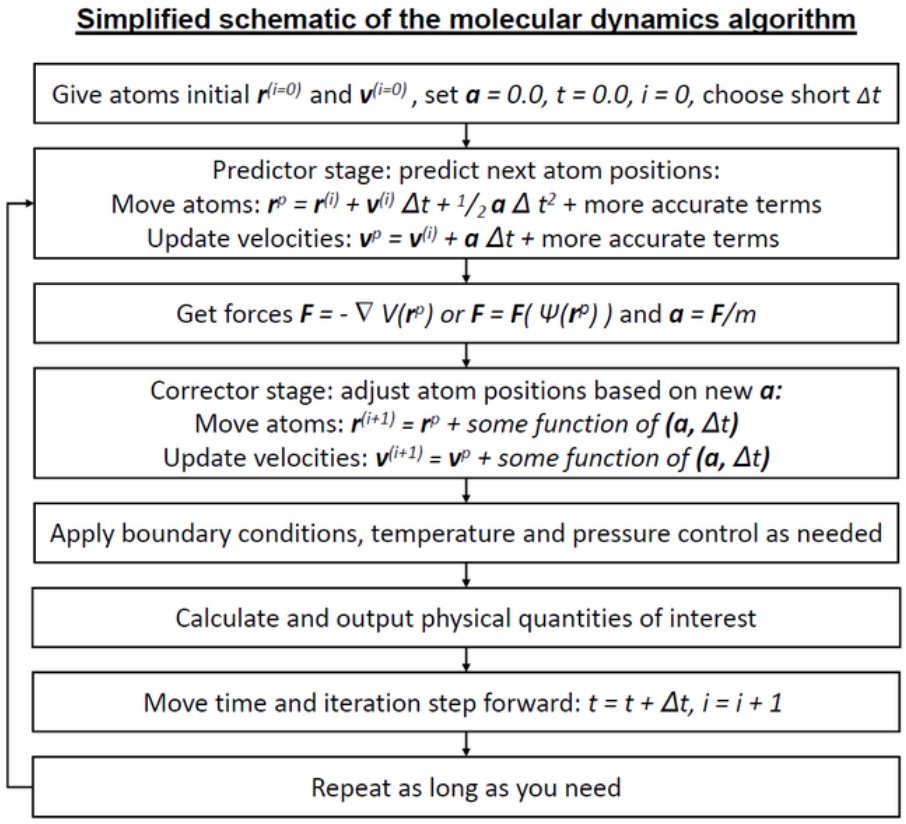

Figure 2. 4 Molecular Dynamics algorithm [117]

Substituting Eq. (2.04) and (2.05) into (2.03), we get:

$$\frac{\mathrm{d}^2\mathbf{r}_i}{\mathrm{d}t^2} = -\frac{1}{m_i}\nabla U_i \tag{2.06}$$

The Velocity-Verlet algorithm is then adopted to perform the time integration and evaluate the new position and velocity of the atom *i*. Figure 2.4 illustrates the schematic of the MD algorithm.

2.2.2 Force Fields

As presented in Figure 2.4, the force field is needed to describe the binding energy among atoms within the atomistic system. The accuracy of the force field directly impacts the accuracy of the MD simulation.

The Lennard-Jones (LJ) potential is the most popular potential that models the interaction between two electronically neutral atoms. It takes the form

$$U(r) = 4\epsilon\left[\left(\frac{\sigma}{r}\right)^{12} - \left(\frac{\sigma}{r}\right)^{6}\right] \tag{2.07}$$

where $U(r)$ is the interatomic potential energy, r is the distance between the atoms, constant σ is the distance at which the potential energy is zero, and ϵ is the potential well. The first term presents the repulsive interaction between two atoms. The second term presents the attractive interaction between two atoms. With the increasing of r, both terms approaching zero. Therefore, a cutoff of distance is defined to reduce the computational cost of the trivial energy calculations.

Similar to the LJ potential, the Morse potential describes two body interactions using three parameters such that

$$U_M = D_M\left[1 - \mathrm{e}^{-\alpha(r-R)}\right]^2 \tag{2.08}$$

Where U_m is the potential energy, D_M is the well depth, R is the equilibrium separation distance, and α is the potential width.

In general, LJ potential is simple and fast without the capability to account for the multi-body interaction within the atomistic system. For metallic system, LJ potential cannot adequately capture the local environment dependence of the electron density and correspondingly, the cohesive energy. Therefore, it is good for qualitative characterization of the material behavior but has a lack of accuracy. To overcome this shortcoming, Baskes and Daw developed the embedded-atom model (EAM) [86]. The potential energy E_i of atom i is defined as

$$E_i = F_i(\rho_i) + \frac{1}{2}\sum_{i \neq j} \phi_{ij}(r_{ij}), \tag{2.09}$$

$$\rho_i = \sum_{i \neq j} f_j(r_{ij}). \tag{2.10}$$

The first term in equation (2.09) is the embedding energy term and the second represents the pair interactions. The variable ρ_i is the local electron density at atom i. The contribution to the electron density at atom i by atom j is described by the function f. Hence summing all contributions (equation (2.10)) gives the total electron density at i. F_i is the energy of embedding an atom in an electron environment defined by ρ_i. In the second term, $\phi_{ij}(r_{ij})$ is the pair potential between atoms i and j, and r_{ij} is the distance between atom i and atom j.

EAM potentials are semi-empirical. All the parameters are fit to the quantum mechanics theory calculation results and experimental data such as cohesive energy, lattice constants,

and elastic constants. They are good for close packed systems such as face centered cubic (FCC), body center cubic (BCC), and hexagonal closed packed (HCP) structures. The EAM potential assumes directional independence of the electron density. It is not suitable for systems with directional bonds as is the case with covalent bonds and transition metals with partially filled *d*-orbitals. A modified embedded atom method (MEAM) was developed as an extension of the EAM that includes an angular term to account for the directional bonding [87]. In the MEAM formulation, the total energy of the system is given by

$$E=\sum_i \left[F_i(\rho_i)+\frac{1}{2}\sum_{j\neq i} S_{ij}\,\phi_{ij}(r_{ij}) \right] \tag{2.11}$$

$$F_i = AE_c \frac{\rho_i}{\rho^0}\log\frac{\rho_i}{\rho^0} \tag{2.12}$$

where A is an adjustable parameter, E_c is the cohesive energy, and ρ^0 is the electron density scaling parameter (ρ^0=12 for FCC) [88]. The background electron density at atom i, ρ_i, is a function of partial electron densities which contain the angular information. The electron density is given by

$$\rho_i = \frac{2\rho_i{}^{(0)}}{1+\exp\left[-\sum_{s=1}^{3} t_i{}^{(s)}\left(\frac{\rho_i{}^{(s)}}{\rho_i{}^{(0)}}\right)^2\right]}. \tag{2.13}$$

Here, s=1,2,3, $t_i^{(s)}$ are weight factors, and the partial electron densities are

$$(\rho_i^{(s)})^2 = \sum_{j,k\neq i} \rho_j{}^{a(s)}(r_{ij})\rho_k{}^{a(s)}(r_{ik})L^{(s)}(\cos\theta_{jik}), \tag{2.14}$$

where θ_{jik} is the angle between the atoms j, i, and k centered at atom i, $L^{(s)}(z)$ are Legendre polynomials and

$$\rho_j{}^{a(s)}(r_{ij}) = S_{ij}f_c(r_{ij})f_j{}^0 \mathrm{e}^{-\beta_j{}^{(s)}\left(\frac{r_{ij}}{r_j{}^0}-1\right)}, \tag{2.15}$$

where S_{ij} is the screening function between atoms i and j, f_c is a cutoff function, and $\beta^{(s)}$ (decay length), f^0, and r^0 are parameters.

2.3 Monte Carlo Simulations

Generally, Monte Carlo simulation refers to any computational methods to solve problems using random generators. The term itself was coined by Metropolis and Ulam while working at Los Alamos in the 1940s, after the gambling casinos in Monte Carlo, Monaco [89]. Ulam had initially used the method to calculate the probability of winning the card game Solitaire. Neumann later used this statistical sampling technique to model neutron diffusion during a thermonuclear reaction [90].

In atomistic simulations, Monte Carlo methods are used to obtain thermodynamic properties of a system by rigorously sampling the configuration space. Depending on the problem of interest, different ensembles can be implemented to model the proper physics of the system. Compared to the MD simulation method, MC simulation method is more suitable for material system equilibration modeling involving slow diffusion processes

[91]. Both techniques use the same system setup wherein particles occupy sites, and potential energy is derived from the force field.

Lattice gas model is generally adopted in the MC simulation. In this model, configurations are obtained by random walks in the phase space that involves random perturbations of the system (particle translations, molecule rotations). New configurations will be accepted based on the Metropolis sampling algorithm to yield a properly Boltzmann-weighted averages for structure and thermodynamic properties [92]. Sampled states form a Markov chain where each state depends on the previous [93]. Moves from state i to new state j carry a probability $\alpha(i \rightarrow j)$ where the stochastic matrix of attempt probabilities satisfies [93]

$$\alpha(i \rightarrow j) = \alpha(j \rightarrow i) \tag{2.16}$$

Moves are accepted with probability

$$P_{\text{accept}}(i \rightarrow j) = \min\left[1, \frac{\rho^{\text{eq}}(j)}{\rho^{\text{eq}}(i)}\right], \tag{2.17}$$

where ρ^{eq} is an equilibrium density set by the equilibrium ensemble. The current state is kept if the proposed new state is rejected. Ultimately, the generated Markov chain of states asymptotically samples the probability distribution ρ^{eq} [93]. Due to the time independence of the method, only static properties can be computed. The only constraints on the moves are that they generate the desired ensemble, and this is guaranteed by the acceptance rules [94]. A sample MC move is shown on the left panel in Figure 2.5. While MD moves result in atoms moving about their lattice points in shorter steps due to the energy barriers, MC random walks allow the system to reach equilibrium even if the stating configuration is far

away from equilibrium for MD to sample. The lattice gas model is originally designed to sample the canonical ensemble but can be extended to other ensembles as discussed below.

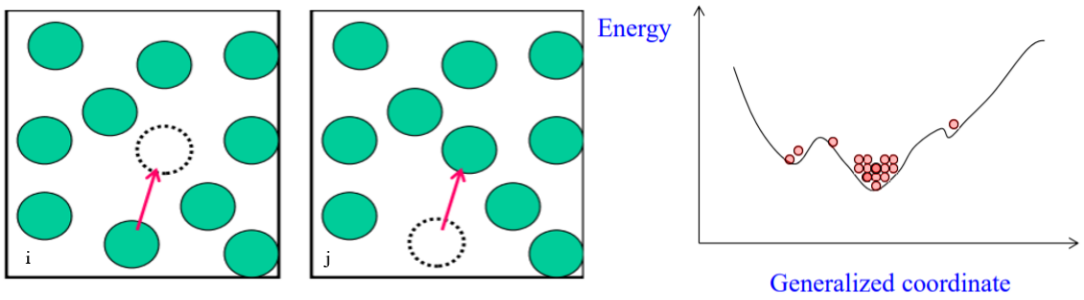

Figure 2. 5 (a) movement of an atom in consecutive MC steps, and (b) the evolution of energy with different sampled configurations. [95]

2.3.1 Canonical Ensemble

The canonical ensemble models an isolated system whose volume, temperature and number of particles are constant. A new configuration can be achieved by randomly moving a particle with a displacement $\delta r_{min} < \delta r < \delta r_{max}$ or switching the position of a pair of atoms with different element types under the original configuration otherwise swapping the same element type would not change the energy of the system. The energy of the new configuration (E_n) is computed and compared with the original configuration (E_o). The new configuration is accepted when the Boltzmann probability

$$P(r) = \mathrm{e}^{\left(-\frac{E_n - E_o}{k_B T}\right)} > \eta \tag{2.18}$$

where k_B is the Boltzmann constant, T is the temperature, η is a random number between 0 and 1.

2.3.2 Isobaric-Isothermal Ensemble

In the isobaric-isothermal ensemble, the number of particles, pressure and temperature are kept constant, but volume changes are allowed in addition to the random displacement moves. These small volume change, δV, is in the range [δV_{min}, δV_{max}]. The new volume at configuration n is thus $V_n = V_o + \delta V$, where V_o is the volume of the original configuration. Atom positions are scaled to the new volume. The modified acceptance criteria is

$$P_{\mathrm{acc,o\rightarrow n}} = \min\left\{1, \exp\left[N\ln\left(\frac{V_n}{V_o}\right) - \beta\Delta U - \beta P\Delta U\right]\right\} \tag{2.19}$$

where $\Delta U = E_n - E_o$, N is the number of atoms, β is reciprocal temperature and P is pressure.

2.3.3 Grand Canonical Ensemble

The grand canonical ensemble (μVT) describes a system in contact with a reservoir of the same particles at temperature T and chemical potential μ. The volume remains constant but particles are exchanged between the system and the reservoir. Therefore, particle displacement, insertion and deletion are permitted. Particle displacements are accepted similar to the canonical ensemble. For additions, a particle is inserted at a random location with the move accepted with probability

$$P_{\mathrm{acc},\, o\rightarrow n}=\min\left\{1,\exp\left[-\beta\Delta U+\beta\mu'+\ln\left(\frac{V}{N+1}\right)\right]\right\} \tag{2.20}$$

where $\mu' = \mu - k_B T \ln\lambda^3(\mathrm{T})$. $\lambda(T)$ is the thermal de Broglie wavelength given by

$$\lambda(T)=\left(\frac{h^2}{2\pi m k_{\mathrm{B}} T}\right)^{\frac{1}{2}} \tag{2.21}$$

where h is Planck's constant, and m is the mass of a particle.

Deletions are accepted with probability

$$P_{\text{acc, o}\to\text{n}}=\min\left\{1,\frac{N}{V}\exp[-\beta\Delta U-\beta\mu']\right\} \tag{2.22}$$

Insertions and removals are conducted with equal probability. The Grand Canonical ensemble has been used to model the adsorption of atoms or molecules of elements [96], depletion interactions in colloidal suspensions [97], the equilibria of ionic solutions separated by a semipermeable membrane [98], and the segregation of interstitial solutes and vacancies in crystalline materials [99].

2.3.4 Gibbs Ensemble

Developed by Panagiotopoulous in 1987 [100], the Gibbs ensemble was introduced as a method to simulate phase coexistence in fluids of pure components or mixtures without a partition. A system is divided into two regions with different densities and compositions and the goal is to achieve chemical equilibrium between the phases. The total number of particles, and overall volume are conserved. A thermal reservoir keeps the temperature of both regions constant. Three kinds of moves are permitted: random particle displacements, particle and volume exchanges between the two phases. In the first type of move, particles in either of the two regions, or both, are displaced with acceptance probabilities similar to the canonical ensemble. The second type of move involves a change in volume of the two regions at constant volume. An increase in the volume of one region is matched by an equal volume decrease of the other. Particle positions are scaled to the new volumes. Based on

the probability distribution for the ensemble, the acceptance criterion for a volume change (ΔV) between two regions, A and B, is

$$P_{\mathrm{acc},o\to n} = \min\left\{1, \frac{(V_A + \Delta V)^{N_A}(V_B - \Delta V)^{N_B}}{V_A^{N_A} V_B^{N_B}} \mathrm{e}^{-\beta\Delta U_A - \beta\Delta U_B}\right\} \tag{2.23}$$

where V_A, V_B are the initial volumes. ΔV is randomly chosen from a fixed range. During particle exchanges, a particle is deleted from one region and inserted in the other. The acceptance criteria for moves from A to B

$$P_{\mathrm{acc},o\to n} = \min\left\{1, \frac{N_A V_B}{(N_B + 1)V_A} \mathrm{e}^{-\beta\Delta U_A - \beta\Delta U_B}\right\} \tag{2.24}$$

and for moves from B to A

$$P_{\mathrm{acc},o\to n} = \min\left\{1, \frac{N_B V_A}{(N_A + 1)V_B} \mathrm{e}^{-\beta\Delta U_A - \beta\Delta U_B}\right\} \tag{2.25}$$

2.3.5 Semi-grand Canonical Ensemble

The Gibbs ensemble is ideal for fluid-fluid phase equilibria studies. However, due to its reliance on successful particle insertions to achieve equilibrium, this ensemble cannot simulate phase equilibria in dense or crystalline solids [101]. A variation of this ensemble, the Semi Grand Canonical (SGC) probes phase equilibria in multicomponent systems (fluid-solid systems) that are not separated by a partition. In the SGC ensemble, the total number of particles, volume, and chemical potential differences are specified. The chemical composition can fluctuate. Instead of insertions, species types are changed under the chemical difference. For each trial, the change in potential energy and concentration are calculated. Trial moves are accepted with probability

$$P_{\mathrm{acc},o\to n} = \min\left\{1, \mathrm{e}^{-\beta\Delta U+\Delta\mu N\Delta c}\right\}, \tag{2.26}$$

where D*c* is the change in concentration.

2.4 Hybrid MC and MD Simulations

As described previously, all atoms are moved simultaneously in MD whereas in MC a few atoms may be moved to maintain high acceptance rates [102]. MD moves are limited by timestep to conserve the total energy while MC moves can be large and unphysical [102]. Hybrid MD/MC combines both MD and MC to create global moves, instead of just localized moves of MD. MD runs are interrupted a specified interval to carry out MC moves. Configurations at the end of MD runs are accepted or rejected based on the Metropolis criterion [103]. Consequently, trials move across sample space in larger steps, and the correlation between successive steps is reduced [102].

2.5 Force Field Selection

As discussed before, force field of the material system need to be carefully selected to accurately capture the material behavior in the MD simulation. While several interatomic potentials have been developed for binary and ternary systems such as Fe-Ni-Cr by Bonny *et al.* [104] and Zhou *et al.* [105], few potentials exist for quaternary and quinary alloys. Zhou *et al.* developed an EAM database tool that allows for the development of an EAM potential file for any combination of the 16 metals Cu, Ag, Au, Ni, Pd, Pt, Al, Pb, Fe, Mo, Ta, W, Mg, Co, Ti, and Zr [42]. Elemental parameters are fitted to basic material properties such as lattice constants, elastic constants, bulk moduli, vacancy formation energies, and sublimation energies. Such potentials have been used to simulate some HEAs. The accuracy of the potential models depends on the accuracy of the elemental parameters. Xie

et al. [106] used the combination of EAM and LJ potentials to model the deposition of AlCoCrCuFeNi thin films on Si and the subsequent annealing process. Several studies have focused on the effect of Al concentration on the phase formation and hardness of AlCoCrFeNi [107] [108] and its compressive properties. For example, varying the molar ratio of Al in as cast $Al_xCoCrFeNi$ results in the following phases: (1) FCC for $0 \leq x \leq 0.375$, (2) FCC–BCC for $0.50 \leq x \leq 0.75$, and (3) BCC for $0.875 \leq x \leq 2.00$ which correspond to an increase in strength hardness [39]. Li *et al.* [109] studied the mechanical behavior of AlCrFeCuNi high-entropy alloys under uniaxial tension using Morse potential and EAM potentials. Interactions of Cr-Fe-Ni, Cu-Cu, and Al-Al are described by EAM potential, and the remaining interactions are modelled using the Morse potential. Such hybrid potentials may not accurately capture the physics of alloy systems as they are not parameterized to the net effect of the mixtures.

Therefore, we test out a few available hybrid potentials and the corresponding HEAs. The objective is to identify an HEA system and a trustable hybrid potential which can be adopted for the GB segregation study in this work.

2.5.1 CoCrFeNi using EAM potential

We combined the EAM parameters of Co-Fe-Ni from Zhou's database and the EAM parameters of Cr from Zhang *et al* [83] to create an EAM potential to study CoCrFeNi HEA. Zhou's database does not include Cr. Large-scale Atomic/Molecular Massively Parallel Simulator (LAMMPS) was adopted to perform the molecular dynamics simulations. The initial system contains 121,000 atoms arranged as FCC lattice in a 10×10×10 cubic cell. The lattice constant is 3.572 Å [76]. The HEA is constructed by

putting Co, Cr, Fe or Ni atoms to the available sites through a 'set' command, which uses random number generators to set the atom type for a specified fraction of atoms in a group. Periodic boundary conditions are applied. Under the NPT ensemble with pressure of 1atm and temperature of 300K, the initial FCC HEA CoCrFeNi structure is diffused into a combination of FCC, BCC and HCP structure, shown in Figure 2.6. Since experiments have confirmed the FCC structure of CoCrFeNi HEA [84], this potential cannot accurately predict the phase of CoCrFeNi.

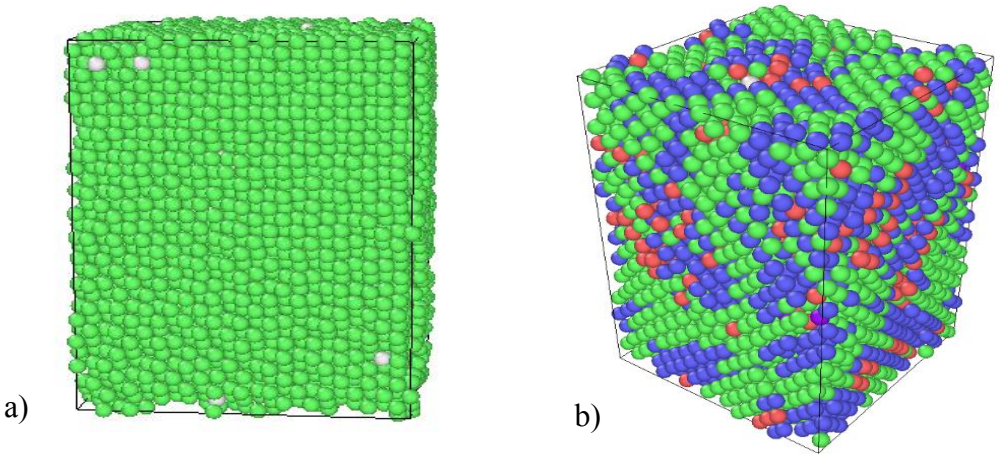

Figure 2. 6 (a) The FCC structure of CoCrFeNi at the beginning of the simulation; (b) a mixed structure of CoCrFeNi at the 0.5ns of the equilibration simulation. Atoms have been colored based on the CNA parameter. Green, blue and red represent FCC, BCC and HCP lattices

To further test out the above EAM potential, uniaxial tensile tests were conducted at different temperatures in the cryogenic range [110]. The BCC CoCrFeNi structure was first equilibrated at the target temperature for around 0.1ns, then it was stretched along the *z* direction at the strain rate of $10^9 s^{-1}$. The pressure in the lateral *x* and *y* directions was kept at 1atm under the NPT ensemble. The stress-strain curves of the HEA at 20K, 40K, 60K, 80K and 100K are shown in Figure 2.7. No significant temperature effect can be observed

with respect to the strength and stiffness of the material. Experimentally, Figure 2.8 presented the stress strain relation of the CoCrFeNi under tensile tests at four different temperatures: 293 K (room temperature), 200 K, 77 K (liquid nitrogen temperature), and 4.2 K (liquid helium temperature) conducted by Liu *et al.* are plotted [110]. The quasi-static strain rate is $10^{-3}s^{-1}$. A clear dependence between mechanical property of materials and temperature can be observed. The yield strength and toughness increase with the decreasing of temperature. Regardless of the difference in strain rate, this EAM potential cannot be used to quantitatively investigate the mechanical properties of the CoCrFeNi HEA.

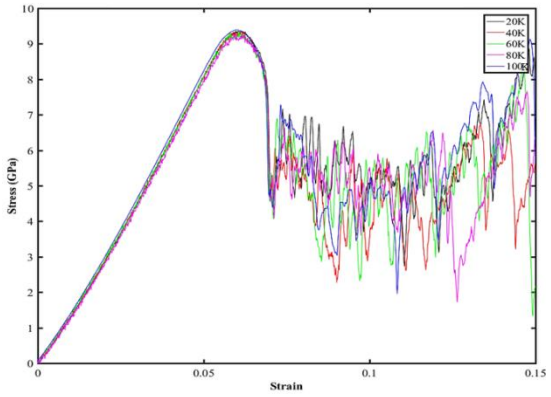

Figure 2. 8 Engineering stress strain curves of CoCrFeNi at different temperatures from MD simulations

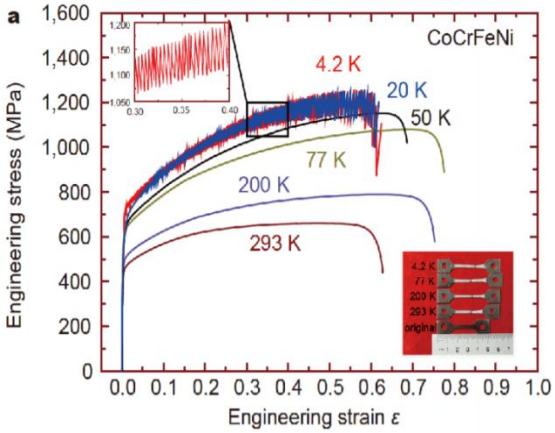

Figure 2. 7 Experimental engineering stress strain curves of CoCrFeNi at different temperatures [110]

2.5.2 AlCoCrFeNi using EAM and Hybrid potential

The EAM database tool by Zhou was then used to create a potential for $Al_xCoCrFeNi$. Experimental findings show that varying the molar ratio of Al in as cast $Al_xCoCrFeNi$ results in the following phases: (1) FCC for $0 \leq x \leq 0.375$, (2) FCC–BCC for $0.50 \leq x \leq 0.75$, and (3) BCC for $0.875 \leq x \leq 2.00$ which correspond to an increase in

strength hardness [57]. In this simulation, we establish a set of initial FCC crystal structures with 10×10×15 unit cells under various Al concentrations x=0, 0.5, 1, 2 where x is the molar ratio. The initial lattice constant is calculated under energy minimization. After equilibrium at 300K and 1atm, uniaxial tensile tests are conducted and presented in Figure 2.9. A decrease trend in strength is observed with the increasing Al content, which is contrary to experimental observations [57]. The crystal structures observed in MD simulation are not consistent with experimental findings as well.

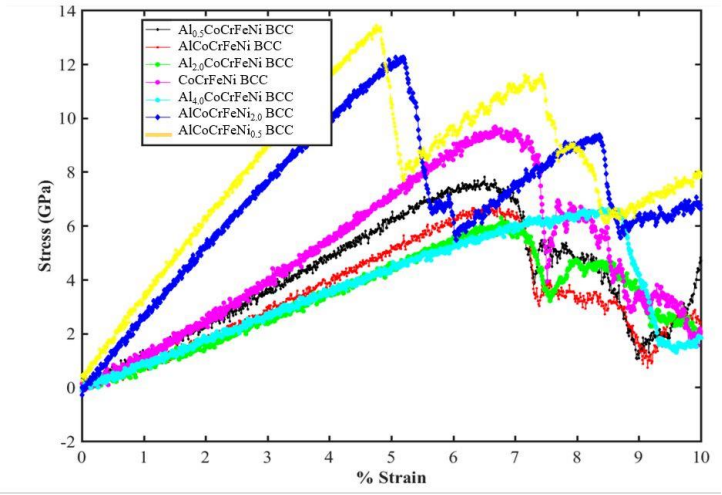

Figure 2. 9 Variation of tensile strength with Al concentration in AlCoCrFeNi using EAM potential

The Cr parameters used in the EAM potential are not part of Zhou's database. Therefore, to check whether the inconsistencies stemmed from incorrect Cr parameters, a hybrid potential was used. Interactions between Cr and the other elements were described by LJ potential [106]. An EAM potential generated from Zhou's database described the other interactions. After equilibration at room temperature, large localized clustering of all Cr atoms was observed, as shown in Figure 2.10.

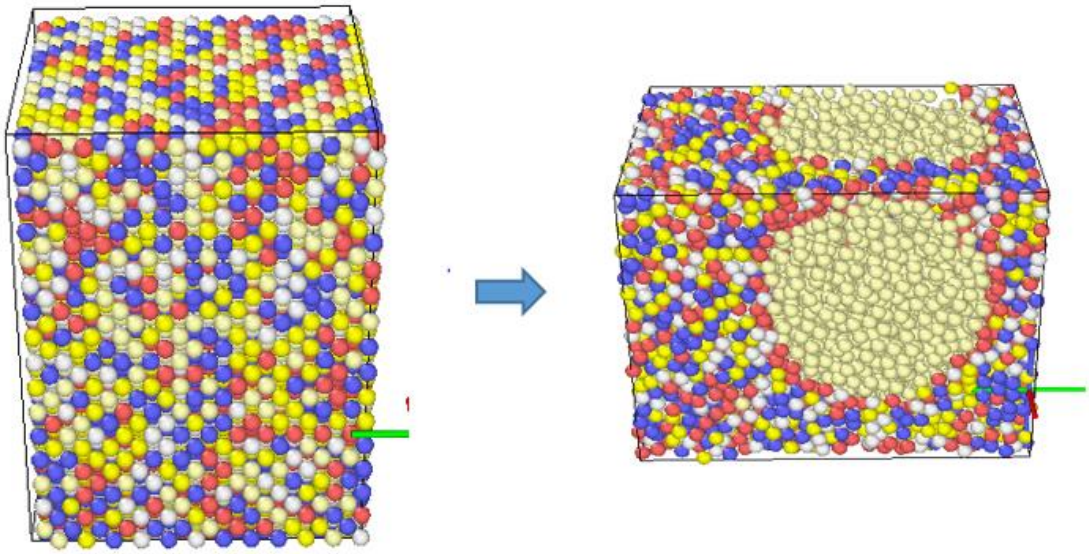

Figure 2. 10 Localized clustering of Cr in AlCoCrFeNi post equilibration using a hybrid EAM-LJ potential

Therefore, both the potential created through the EAM database tool by Zhou and the hybrid EAM/LJ potential for Cr interaction cannot be adopted to study AlCoCrFeNi HEA.

2.5.3 CoCrFeMnNi

A new MEAM interatomic potential for the Cantor alloy was recently developed [111] by Choi *et al.* As the only potential that describes the interactions in CoCrFeMnNi, this potential yields a stable FCC lattice and also reproduces the formation of twins at low temperatures which is characteristic of the HEA. The potential has been used to study the impact of grain size on melting temperature and tensile strength [112], and radiation damage [113]. We established a CoCrFeMnNi FCC lattice with the size of 20Å$\times$20Å$\times$ 20Å. Energy minimization calculation is conducted with an energy tolerance of 10^{-24} eV and force tolerance of 10^{-24} eV/Å. Potential energy per atoms is plotted with respect to lattice constant, shown in Figure 2.13. The red line is the running average computed every

10 data points, and the cyan line is the lattice constant corresponding to the minimum binding energy per atom. At 0K, the lattice constant of CoCrFeMnNi is 3.591Å, close to the experimental value of 3.59Å obtained from XRD experiments extrapolated to 0K [114].

The potential also resulted in a stable FCC structure for temperatures up to 600K.

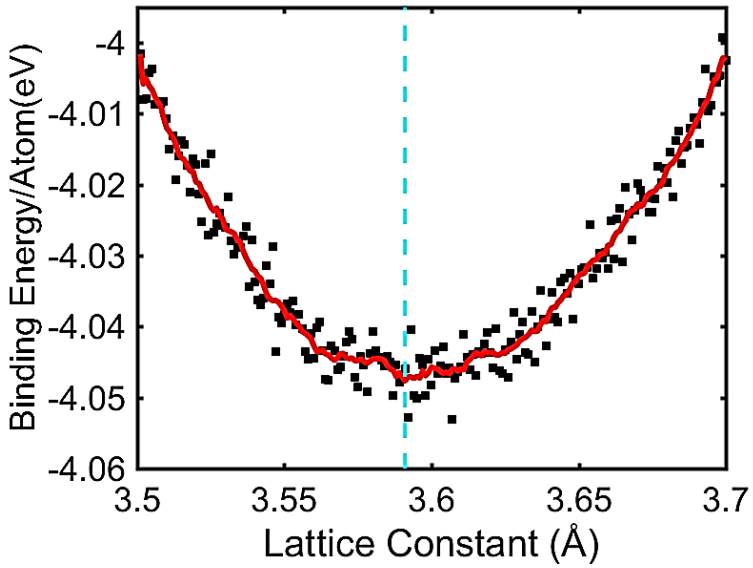

Figure 2. 11 Cohesive Energy per atom versus lattice parameter of CoCrFeMnNi. The cyan line marks the lattice constant of 3.591Å

Therefore, we adopt this MEAM potential to study CoCrFeMnNi in the following investigation.

2.5.4 Summary and potential selection

We have tested the available force fields for three HEAs: CoCrFeNi, AlCoCrFeNi, and CoCrFeMnNi. It turns out the new MEAM interatomic potential for the Cantor alloy developed [111] by Choi *et al* is capable to accurately predict the phase and lattice constants of CoCrFeMnNi. Therefore, we will adopt this potential to investigate the role of GB segregations of bi-crystal CoCrFeMnNi HEA in the following study.

2.6 Simulation Setup

In order to study the GB segregation of CoCrFeMnNi, we adopted GB Studio to create a bi-crystal symmetric tilt ∑5 (3 1 0)[0 0 1] FCC lattice with a misorientation angle θ=36.9^{o} , containing 112,000 atoms in a box of dimensions 7.2nm$\times$8.0nm$\times$22.7nm. The lattice constant is 3.591Å. A cutoff distance 1.5 Å is selected to remove the duplicate atoms at the GB interface during the formation process of the bi-crystal structure. After the bi-crystal FCC lattice is established, we adopt the method described in Chapter 2.5.1 to construct the equimolar HEA CoCrFeMnNi. Energy minimization method is then adopted to reach to a relaxed configuration.

2.7 Post-processing techniques

2.7.1 Common Neighbor Analysis

The Common Neighbor Analysis (CNA) method was proposed by Honeycutt and Andersen as a way to identify crystal structures [115]. Atom pairs are assigned indices based on (i) whether or not they are nearest-neighbors, (ii) the number of common neighbors they share, and (iii) the number of bonds between these common neighbors. Four indices are included. The first index is either 1 if a pair of atoms are near neighbors, or 2 if they are not. A near neighbor lays within a cutoff radius defined by the first peak on the radial distribution function. The second number is equal to the number of shared neighbors, and third index is a count of the bonds between any of the neighbors. A fourth index is assigned to distinguish diagrams with similar first three indices such as FCC and HCP. Figure 2.12a presents the 1421 diagram in FCC which each pair *i* and *j* has 4 common neighbors and 2 bonds between them. Figure 2.12b shows the 1422 diagram

found in the HCP structure. The 1441 diagram and 1661 diagram found in BCC structures are shown in Figures 2.12c and 2.12d, respectively. An FCC atom will have all its bonded pairs with index IDs 1421, HCP has half 1421 pairs and half 1422 pairs. The BCC structure has 8 atom pairs forming the 1661 diagram and 6 pairs forming the 1441 diagram. This algorithm is implemented in LAMMPS [116] and OVITO [118] assigns 1 for FCC, 2 for HCP, 3 FOR BCC, 4 for icosahedral and 5 for unknown crystal structures. In a single solid bicrystal, atoms in the bulk are identified as a uniform crystal type (FCC in this case) while the boundary atoms are tagged as non-FCC.

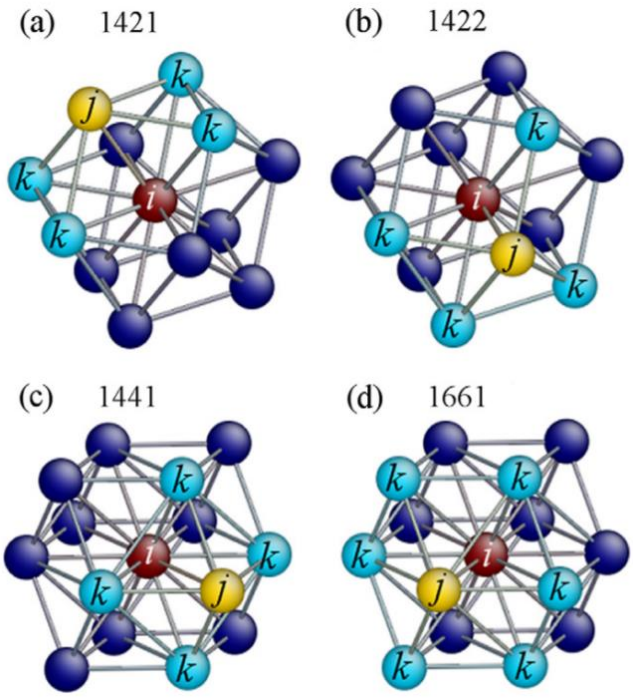

Figure 2. 12 Classification of crystal structures based on the CNA method. Atoms *i* and *j* form the pair and the blue atoms are their nearest neighbors. Green atoms (k) are the common neighbors for the atom pair. The numbers indicate the signatures present in common crystal structures described above [115].

2.7.2 Radial Distribution Function (RDF)

The radial distribution function or pair correlation function, g(r), describes how the atomic density varies with respect to the distance from a reference atom. By definition, it quantifies the unnormalized probability per unit volume of finding a particle at a distance *r* from the reference particle. It is given by

$$g(r)=\frac{1}{N}\frac{dn(\mathrm{r})}{4\pi r^2 dr\rho} \tag{2.32}$$

where N is the total number of particles, $dn(r)$ is the number of particles inside a shell between r and $r+dr$. The number density $\rho = N/V$. Figure 2.13 shows how the RDF is determined for the blue reference by counting the green atoms inside the shell.

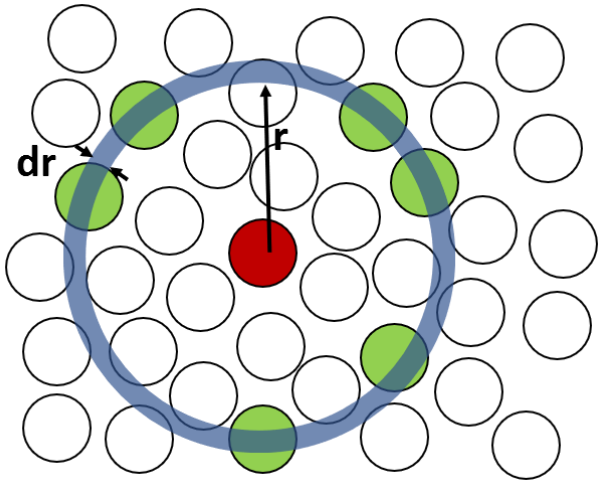

Figure 2. 13 Schematic for the computation of a radial distribution function of a single particle

A system is first divided into bins (shells) and the RDF of each particle is computed and averaged based on the selected bin. The number of particles in each bin can be computed at specific intervals during the simulation and time averaged. The RDF

reveals information about the structure of a material (solid, liquid, gas). In a crystalline structure, each peak corresponds to a set of neighboring atoms. For example, the first peak is related with the nearest neighbor atoms, the subsequent peaks are related with the 2^{nd}, 3^{rd} nearest neighbor atoms and so on so forth. As *r* approaches infinity, the RDF is approaches unity. Experimentally, the RDF can be obtained from X-ray diffraction data by applying a Fourier transform [119].

2.7.3 Dislocation Extraction Algorithm

In addition to identifying the phase of crystal structures, it is also crucial to identify defects such as vacancies, interstitials, and dislocations. Defect regions can be identified using CNA method since atoms have different lattice structure types at the vicinity of the defect region. However, the CNA method is not sufficient enough to capture the stacking patterns associated with the dislocations within the lattice structure. Therefore, more sophisticated algorithm is necessary to fully characterize the type and Burgers vectors of the dislocations. The Dislocation Extraction Algorithm (DXA) is a robust tool developed by Stukowski and Albe for the geometric characterization of dislocation lines from the atomic coordinates of any crystalline structure [120]. To identify a dislocation line and compute its Burgers vector, a trial circuit is constructed around a potential dislocation. First, Delaunay tessellation is constructed to join all atoms in the system. CNA is used to identify atoms which are not belong to a perfect crystal arrangement. Tessellation edges adjacent to these atoms are tagged as bad. The elements formed by these atoms are called ‘defect mesh’. All dislocations can then be discovered by constructing trial Burgers circuits on this surface. A maximum trial circuit length is

specified in units of atom to atom steps. Circuits resulting in non-zero Burgers vectors are used to discover the rest of the dislocation line. Figure 2.14 shows the elements comprising the defect mesh, and the dislocation line traced from the trial circuits. With this tool, the dislocation length can be calculated which allows for the density to be determined. Dislocations can be classified as perfect dislocation, and partial dislocation, which include Shockley, Stair-rod and Hirth dislocations.

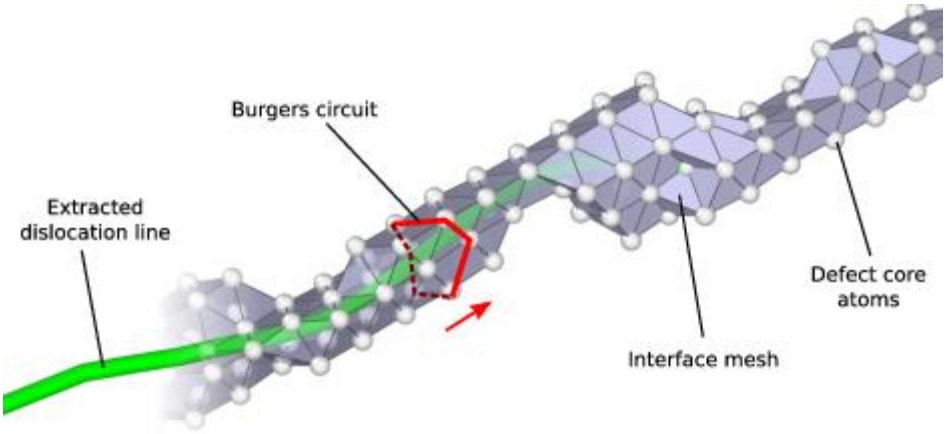

Figure 2. 14 Illustration of the defect mesh constructed with triangular elements. Burgers circuits are drawn on this surface to discover the dislocation line shown in green [120].

2.7.4 Dislocation Density Computation

Dislocation density is defined as the total dislocation length per unit volume. A batch script was executed using OVITO's Python interpreter within the program's graphical interface. The script calls OVITO to open the dump file containing atom trajectories during loading. For each frame, the DXA tool extracts all lattice dislocations and calculates the total dislocation lengths. The system volume is computed, and the density found by dividing the dislocation length by the volume of the simulation system. Based on the frequency at which atom snapshots are exported to the dump file, the strain at each frame can be determined.

2.8 Chapter summary

In this chapter, we briefly introduce the grain boundary definition and characterization, the simulation methods, the selection of the force field and HEA, the simulation setup and the post-processing techniques. In the next chapters, we will investigate the GB segregation and selective doping of CoCrFeMnNi bi-crystal and their impact to the strain-stress relation of the bi-crystal through the uniaxial loading tests.

CHAPTER 3. GRAIN BOUNDARY SEGREGATION WITH SURFACE EFFECTS

In this chapter, we adopt the hybrid MD/MC simulation to investigate the elemental segregation at the grain boundary of a bi-crystal bulk model and a bi-crystal nanowire model.

3.1 Simulation Setup

The initial atomic structure of CoCrFeMnNi HEA with symmetric ∑5 (3 1 0)[0 0 1] θ =36.9° bi-crystal grain boundary is generated by GB studio with the consideration of energy minimization and atom deletion, shown in Figure 3.1. Different type of atoms are equal-molar and uniformly distributed, shown in Figure 3.1 (a). The FCC lattice structure within the grain and the disordered lattice structure at the grain boundary is shown in Figure 3.1 (b). The size of the bi-crystal grain is listed in Figure 3.1 (b) as well.

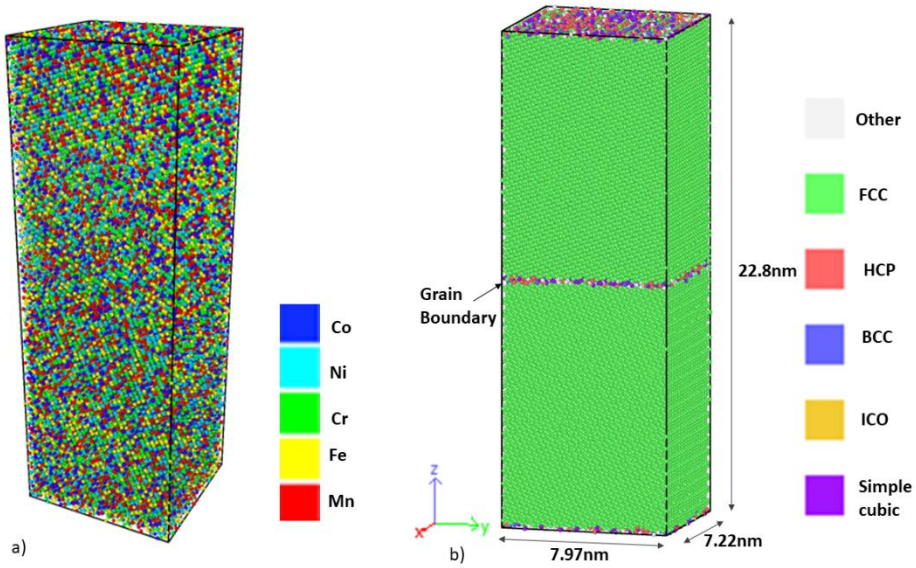

Figure 3. 1 Initial bicrystal setup for the investigation of grain boundary segregation in the HEA. Atoms are colored a) according to the atom type and b) CNA parameter according to the key on the right

Periodical boundary conditions are applied in all three directions. The energy minimization is performed with the conjugate gradient method while the box is allowed to relax. After that, the whole system was heated to 300K at 1atm for 100ps under the Nosé–Hoover thermostat and barostat. The timestep is defined as 0.001ps. The hybrid MD/MC process is then performed at 300K for 5 million-time steps (5ns). During the hybrid MD/MC process, one MC swap calculation runs at every 10 MD steps. In the MC step, every atom is swapped with a random atom of a different type according to the Metropolis algorithm. During the hybrid MD/MC process, the potential energy is decreasing and converging to a more stable energy configuration. The resulting HEA structure is then investigated in the following sections.

3.2 Grain Boundary Segregation of the HEA Bi-crystal Bulk Structure

The potential energy variation during the 5 million MD/MC steps is shown in Figure 3.2. Apparently, the MC swapping process can further reduce the potential energy

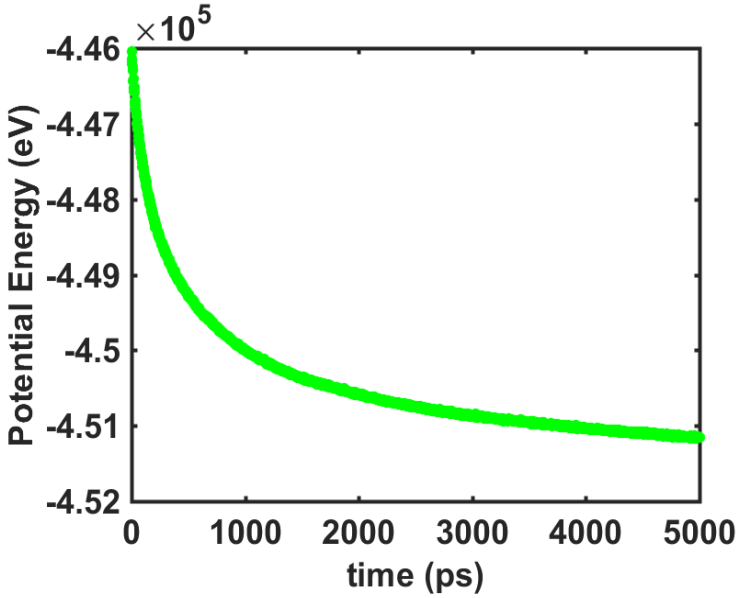

Figure 3. 2 Variation in potential energy during MD/MC steps.

of the HEA system. After 5ns simulation, the potential energy was still decreasing but close to the equilibrium. The system parameters such as dimension, temperature and pressure during the MD/MC process are plotted in Figure 3.3.

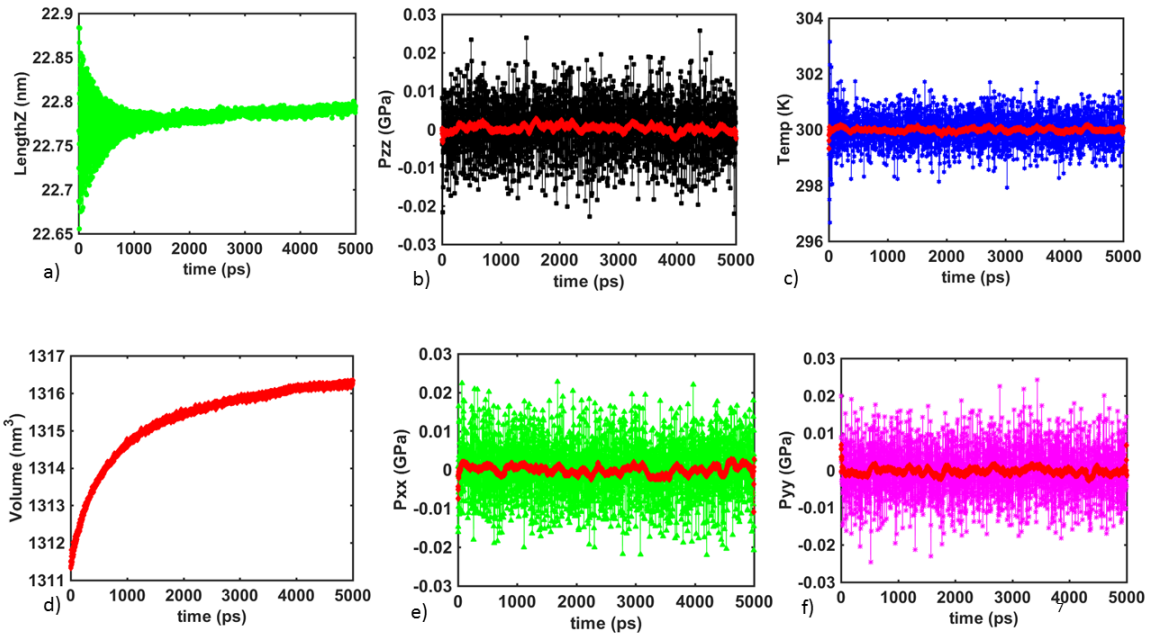

Figure 3. 3 Variation of length, volume, temperature, and pressure components during the MD/MC swapping process

The red lines are the average value of the data with respect to time steps, aimed for the guidance. As can be observed, the temperature and pressure of the system are well maintained during the MD/MC process. The dimension perpendicular to the GB direction is slightly relaxed with the corresponding volume increasing. However, such state can be considered as quasi-equilibrium till the end of 5 million steps MD/MC simulation. It can be adopted for the following GB segregation investigation.

As can be observed in Figure 3.4 (b), the FCC crystal structure of CoCrFeMnNi within the bi-crystal grain is maintained after 5 million steps of hybrid MD/MC calculation. Compared to the initial configuration shown in Figure 3.1(a), localized

clustering of the Cr/Mn (green/red) and Co/Fe (blue/yellow) can be observed within the grain and along the grain boundary, as shown in Figure 3.4 (a).

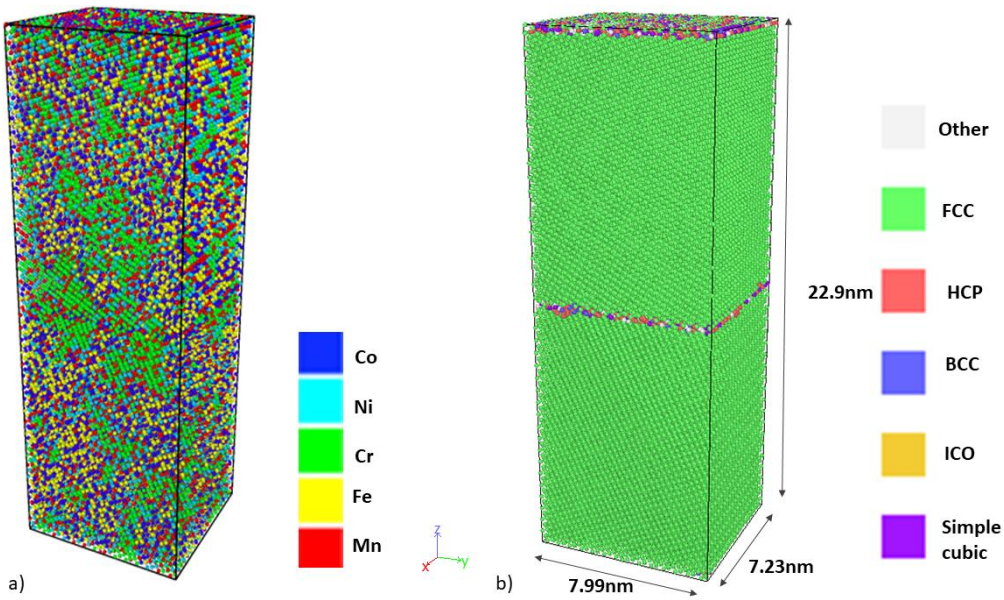

Figure 3. 4 Configuration of CoCrFeMnNi bicrystal structure at 5 million time steps of MD/MC run. Atoms are colored a) according to the atom type and b) according to the CNA parameter.

In order to investigate the GB segregation during the MD/MC process, we first define a group of atoms belonging to the GB by selecting the atoms with the CNA value not equaling to 1 (referring to FCC structure). Out of 120,000 atoms in the bi-crystal structure, there are 2314 atoms at the two GBs, around 1.9% of the total atoms in the system. After sorting each type of elements within the GB group, the GB concentration can be evaluated by dividing the number of atoms of each element type to the total number of atoms within the GB group. A bar graph of GB concentration at the end of the MD/MC, based on the last image, is presented in Figure 3.5 (a). The concentrations of Cr and Mn are increased to 35% and 27% respectively. The concentrations of Fe and Ni are depleted to 5% and 7% respectively. The concentration of Co is not significantly modified. Based

on the atomic radii of the five elements shown in Figure 3.5 (b), we observed that large dopants, such as Cr and Mn, have a tendency to segregate to the GB.

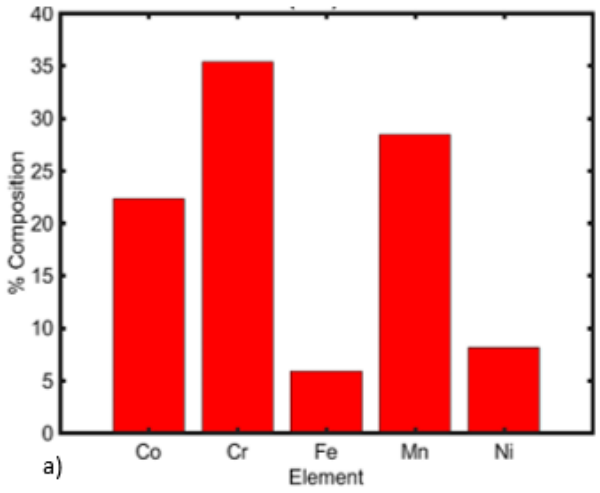

b)

Dopant	Atomic Radius (pm)
Cr	166
Mn	161
Fe	156
Co	152
Ni	149

Figure 3. 5 The elemental concentrations at the GB after the MD/MC process. (b) The atomic radius of the dopants in the CoCrFeMnNi HEA system.

We elucidate the atom arrangement at the GB as well as its local stress distribution. The atom arrangements near GB before MD/MC, and after 5ns MD/MC process are shown in Figure 3.6 and Figure 3.7 respectively. The symmetric ∑5 (3 1 0) [0 0 1] θ =36.9° GB consists of repeating kite shaped structural units. There are 4 unique symmetric sites within each kite shaped structural unit along the GB. As can be observed, the largest Cr atoms

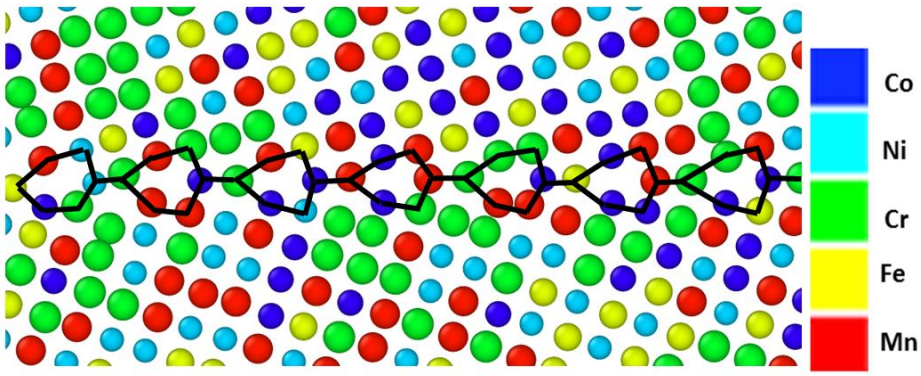

Figure 3. 6 The initial ∑5 (3 1 0) GB structure colored based on atom type .

prefer to occupy site 1 (100% within the observation window) whereas the small Ni atoms prefer site 4 (over 85% within the observation window).

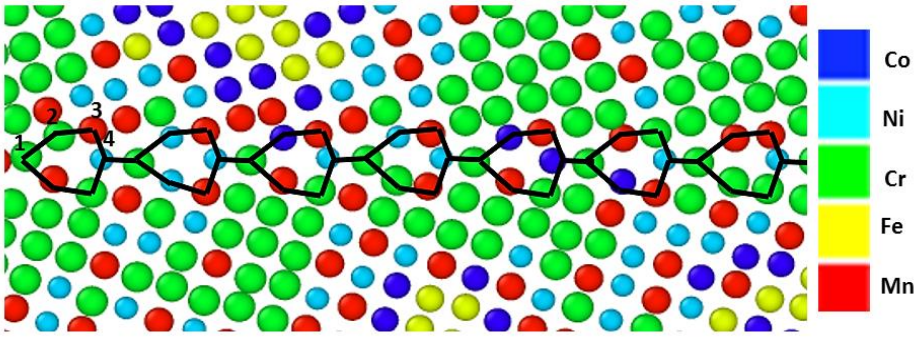

Figure 3. 7 The segregated ∑5 (3 1 0) GB structure colored based on atom type after 5 million time steps in MD/MC simulation.

Following the method of Hu and Rupert [126], the symmetric per-atom stress tensor at each site is calculated. The hydrostatic stress (first invariant of the stress tensor) at each atom is presented in Figure 3.8. Sites in tension are colored in red while those in compression are colored in dark blue. The results confirm that the dopant size is a factor to alter the local stress near the grain boundary. With the consideration of bonding energy among dopants, large element atoms are possible to occupy the large vacant size and small

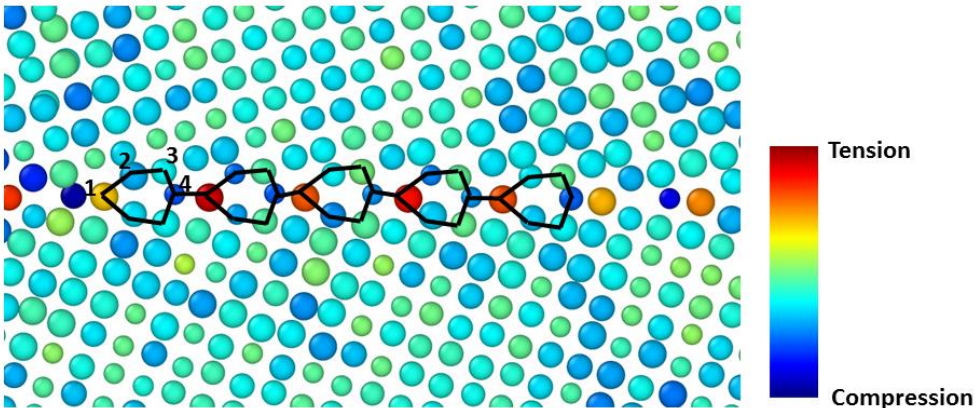

Figure 3. 8 Hydrostatic stress at different grain boundary atomic sites after MD/MC.

element atoms to the small vacant size at the grain boundary, resulting into a lower lattice strain and a lower potential energy.

Since the elemental distribution is alternated at GB, we also evaluate the component distribution within the grain along the direction perpendicular to the grain boundary. Periodic images along *z* direction is considered in order to accurately capture the two GB information of the bi-crystal. A bin size of 1nm is selected along *z* direction to count the elemental concentrations. The elemental concentration along z direction at the initial bi-crystal structure and the current bi-crystal structure after MD/MC process are presented in Figure 3.9 and Figure 3.10, respectively. As shown in Figure 3.9, five elements of the HEA are uniformly distributed with concentration of 0.20±0.15 throughout the HEA, regardless of the grain and grain boundary. However, after 5ns MD/MC process, elemental segregation can be clearly observed at the GB and within the grain, shown in Figure 3.10. A significantly high concentration of Cr and low concentration of Fe can be observed at

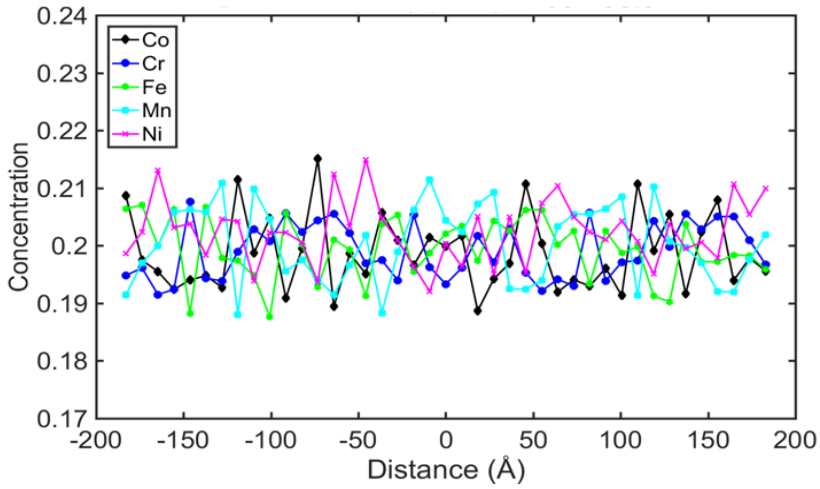

Figure 3. 9 Concentration profiles of the elements in the bi-crystal CoCrFeMnNi supercell at the initial configuration.

the GB. On the other hand, Cr concentration is lowered within the grain and Co/Fe concentrations are raised within the grain. The concentration profile of Ni and Mn is well maintained within the domain, regardless of grain and GB. The mechanism behind such GB segregation will be discussed in Chapter 3.5.

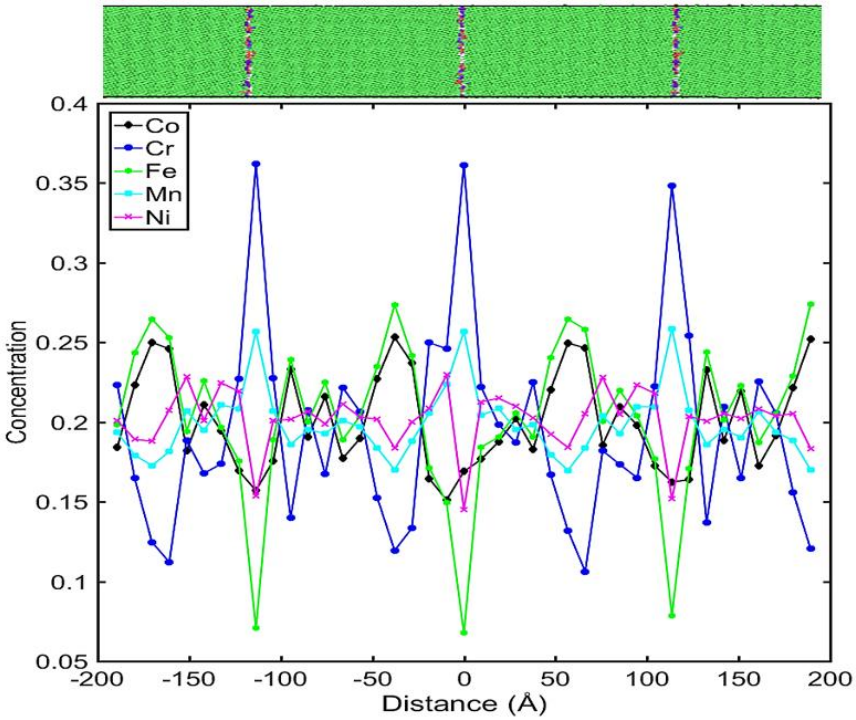

Figure 3. 10 Concentration profiles of the elements in the bi-crystal CoCrFeMnNi supercell at the initial configuration.

3.3 Free surface effects

According to the thermodynamics of the Rice-Wang model of dopant potency, if a solute segregates to a free surface instead of the grain boundary, it will embrittle the GB when placed at the GB interface. Similarly, a dopant that segregates to the GB will increase the strength of the GB [125]. We have observed the elemental segregation due to the abnormal lattice structure at the GB. In this section, we will investigate the possible

elemental segregation due to the missing symmetric at the free surface. To create the free surface, the bi-crystal model in the previous sections is adopted by adding 10nm vacuum space along the lateral *x* and *y* directions. Similar process is conducted to firstly relax the structure with energy minimization method, secondly relax the system at room temperature. Pressure along the *z* direction was kept at 1atm under the NPT ensemble to maintain the vacuum space. The MD/MC swapping process was then carried out under the isothermal-isochoric (NVT) ensemble at room temperature (300K). During the MD/MC swapping process, Mn atoms (red) tends to move to the surface. After 3ns, the free surface of the bi-crystal grain is mostly occupied with Mn atoms, as can be observed in Figure 3.11.

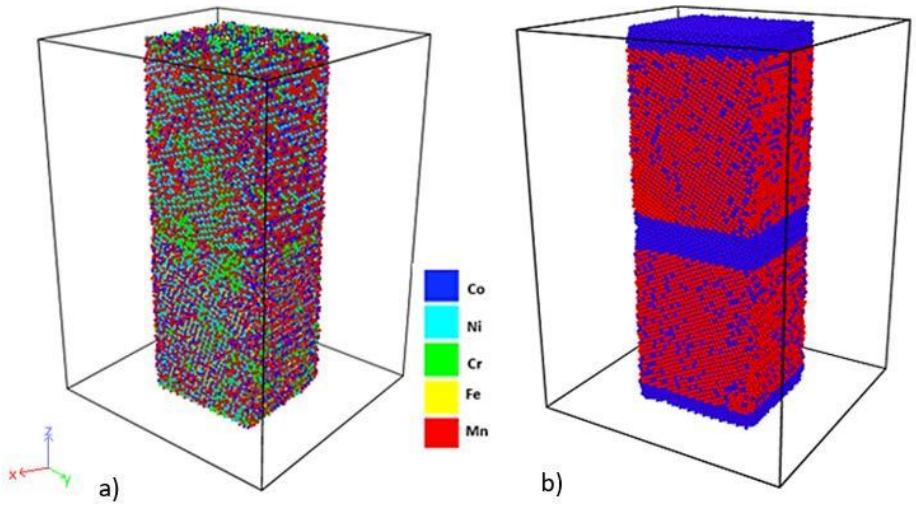

Figure 3. 11 a) Atomic structure of CoCrFeMnNi bi-crystal with free surface after 3ns MD/MC swapping process b) Surface atoms outside the grain boundary defined by shown in red

During the MD/MC swapping process, the potential energy is decreasing as shown in Figure 3.12. Other statistical parameters during the MD/MC swapping process are shown in Figure 3.13. Pressure is well maintained at 1atm with the temperature converging to a constant, which is slightly below the room temperature. The length

dimension in z direction is slightly increased. The final dimensions in the x, y, and z directions were 7.36nm, 8.04nm, and 22.68nm, respectively.

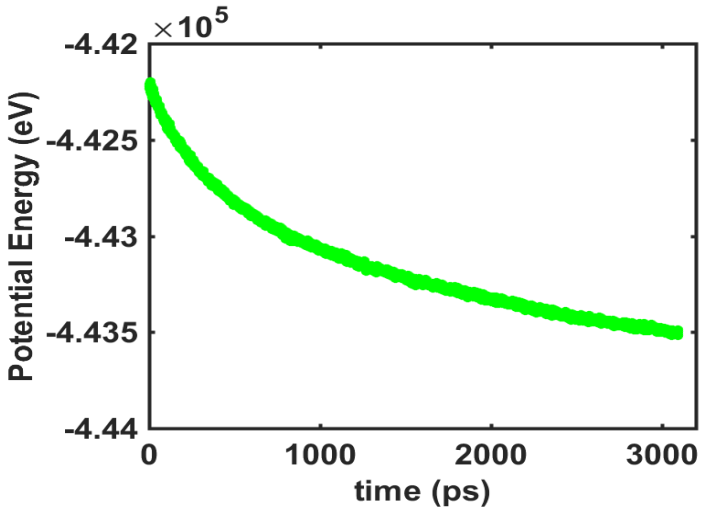

Figure 3. 13 Potential energy during MC+MD equilibration of nanowire HEA.

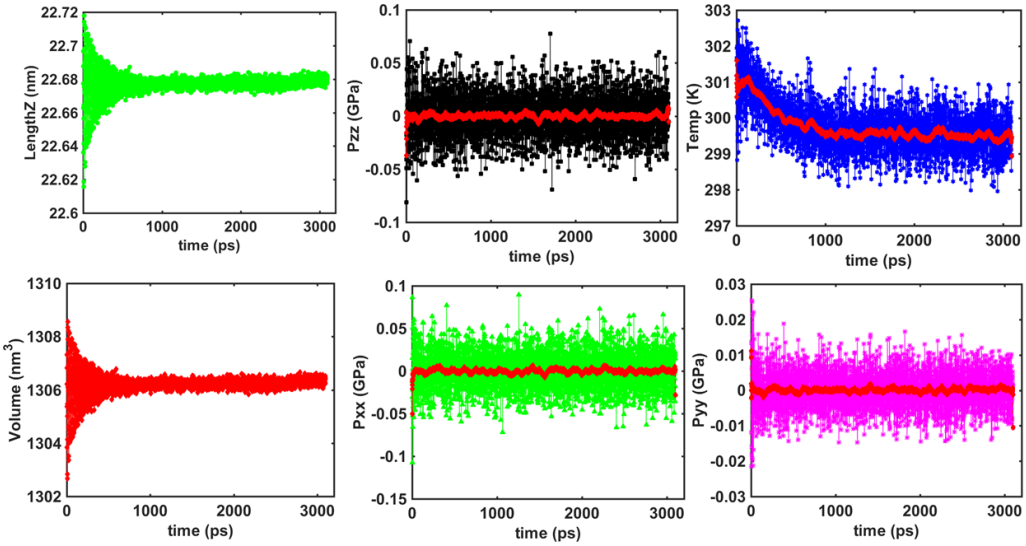

Figure 3. 12 Variation of length, volume, temperature, and pressure components during MC+MD equilibration of nanowire.

To compare concentrations of each element at the surface of the bi-crystal nanowire model, we select all the atoms at the surface of the nanowire outside the grain boundary.

Due to the lack of periodicity in the lateral directions, surface atoms can be identified based on their CNA number in OVITO. Surface layer element concentrations are shown in Figure 3.14.

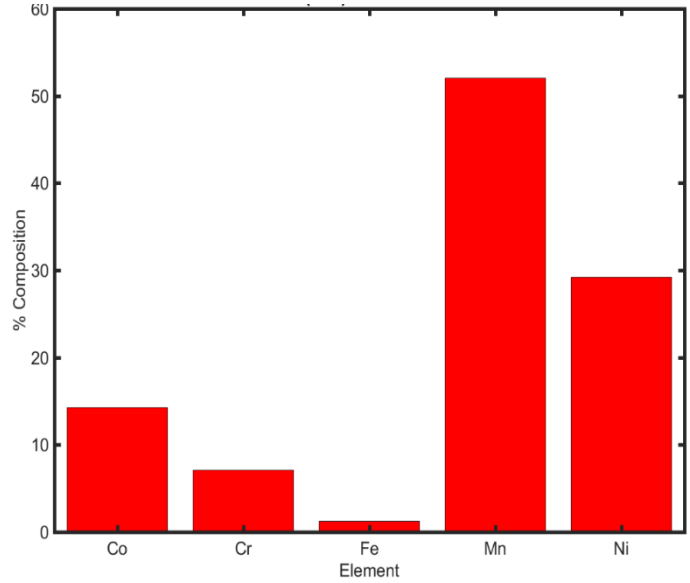

Figure 3. 14 Surface atom concentrations of CoCrFeMnNi bi-crystal

The Mn concentration is as high as 52.0%, much higher than the 28% on the GB, shown in Figure 3.5. It indicates the energetically favorable site of Mn is at the free surface. The Fe concentration is as low as 1.2%, lower than 5% of Fe concentration at the GB. It indicates the energetically favorable site of Fe is at the GB. The Ni, Co, and Cr concentrations are 29.2%, 14.2% and 7.1%, respectively. A similar conclusion would be made that Cr prefers the sites on the GB (35%), rather than the free surface (7.1%).

We also investigate the elemental concentration profile along the longitudinal direction of the bi-crystal, without considering atoms that are with 1.5nm of the lateral surfaces as shown in Figure 3.15. Despite the introduction of free surfaces, the elemental concentration along the longitudinal direction is similar to what has been presented for the

bulk HEA case. However, the Cr and Mn concentration at the GB is lower than that in the bulk HEA case. The Fe and Co concentration within the grain is higher than that in the bulk HEA case.

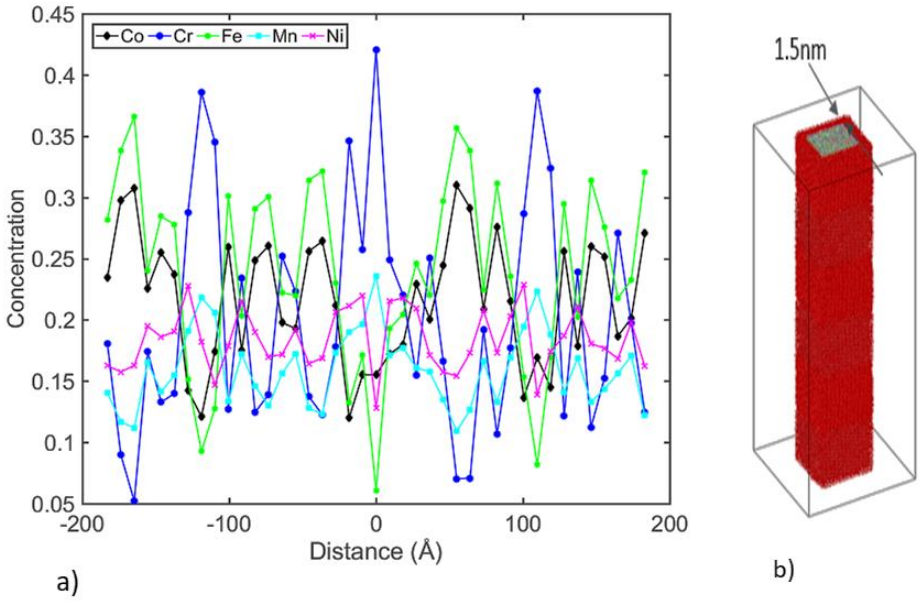

Figure 3. 15 a) Concentration profiles of CoCrFeMnNi nanowire after Monte Carlo simulations excluding surface atoms. b) Surface atoms excluded from the computation are highlighted in red

To further investigate the surface effects, we plot the element concentration profiles along *y* direction (parallel to the grain boundary) with respect to the grain domain and GB domain. As shown in Figure 3.16, the GB domain is defined as 1nm thickness. The domain size of the grain is then defined according. The bi-crystal supercell is divided into multiple bins with the bin size of 1nm in *y* direction. The concentration profiles of the grain region and GB region along *y* axis are shown in Figures 3.16 (a) and (b), correspondingly.

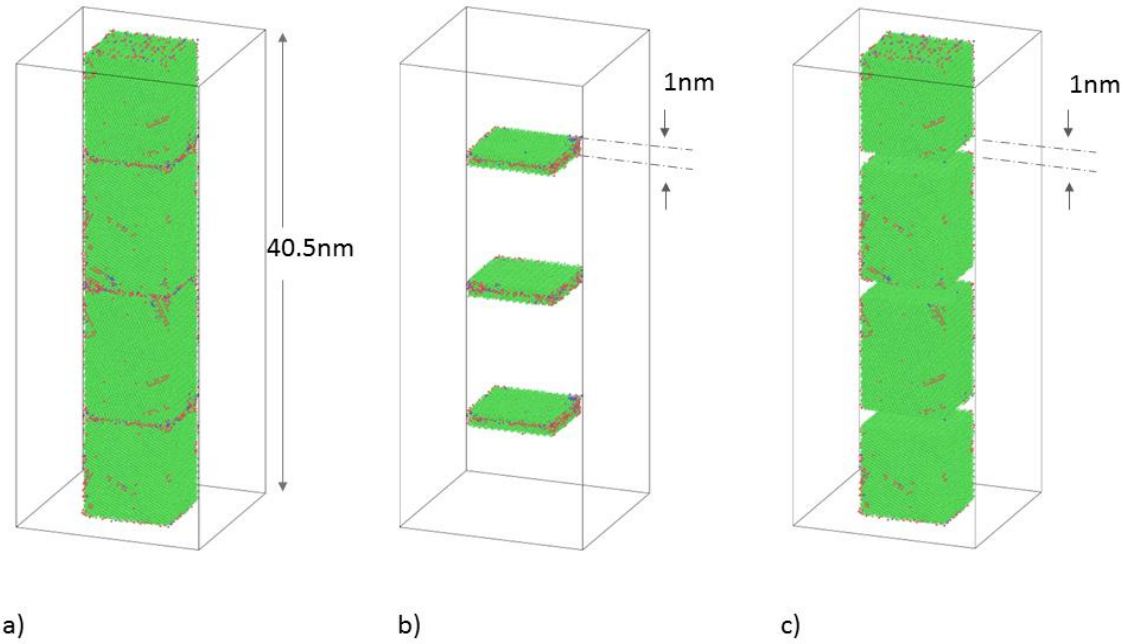

Figure 3. 16 a) Nanowire supercell used for transverse concentration profile plots colored based on CNA. Green atoms indicate FCC atoms and the red atoms are non-FCC. In b) the grain boundary atoms have been isolated and in c) the bulk atoms are shown.

At the surface of the grain domain, Mn has the highest concentration of 27.5% whereas the concentration of Cr is 17.0% and Fe has the lowest concentration at 14%. Cr concentration remains below 18% with increasing distance from the surface while Fe concentration increases to a maximum of 27% in midway between the surfaces. Along the grain boundary however, the concentration of Fe is below 10%. Thus, Fe neither segregates to free surfaces nor grain boundaries. As anticipated, Cr concentration is high throughout the grain boundary. At the intersections between the grain boundary and free surfaces, Cr concentration is 26% and 30.5%. The asymmetry stems from the use of non-periodic boundaries and that the structure is not fully equilibrated. On the other hand, Mn segregates to both the surface and grain boundary. Along the grain boundary, its concentration is 30% at the surface and only drops to a minimum of 22.5% away from

the surface. The presence of Mn at the grain boundary is most likely due to its strong attraction to Cr in the HEA as discussed in the next section. The strong Mn surface segregation is consistent with the findings of Chatain *et al* [121].

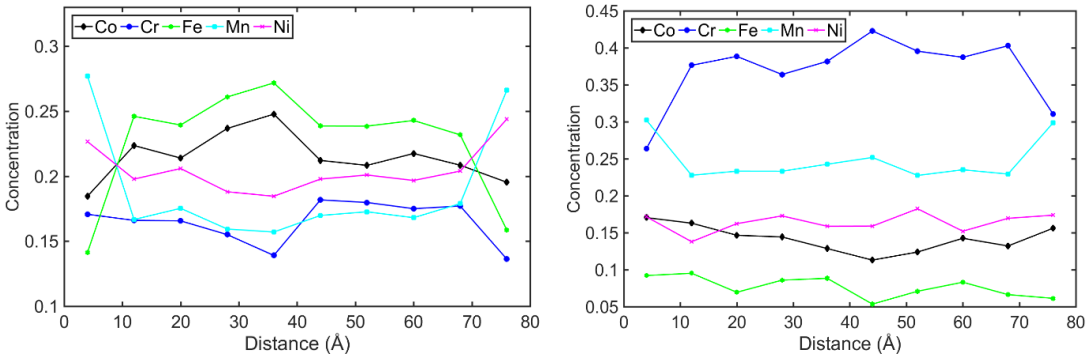

(a) (b)

Figure 3. 17 Element concentration profile along *y* direction within the grain (a), and along the GB (b).

3.4 Energetic Study of the Solute Binding Energy within HEA

We have explained the correlation between GB segregation and the size of solute. Other than GB segregation, we also observed the behavior of solute-solute pairing within the grain and along the GB. For example, Fe and Co always bond with each other and have similar concentration within the grain. Cr and Fe present a repulsive behavior with a contradictory concentration within the grain and along the GB. In order to provide a more in-depth understanding about the solute binding from an energetic point of view, we first plot the radial distribution functions (RDF) with respect to each element, shown in Figure 3.18. Fifteen unique combinations are listed: Co-Co, Co-Cr, Co-Fe, Co-Mn, Co-Ni, Cr-Cr, Cr-Fe, Cr-Mn, Cr-Ni, Fe-Fe, Fe-Mn, Fe-Ni, Mn-Mn, Mn-Ni, and Ni-Ni. Reference atoms are selected in and outside the grain, and neighboring atoms are counted

with the spherical shell thickness of dr=0.04Å. The RDF plots in Figure 3.18 is obtained by time averaging the 100 images of the MD equilibration right after the MD/MC process. RDF g(r) reveals strong short range ordering (SRO) between Cr-Cr, Co-Fe, and Mn-Ni at the first three nearest neighbor. A weak affinity between Cr-Fe and Co-Co is observed as well. Mn has a relatively high affinity with Ni but not strong repulsion with any of the elements within the HEA. Such relation is consistent with what we observed in Figure 3.10. We further perform the static energy calculation to evaluate the solute-solute binding energy within the HEA system by adopting the potential as described before. Since HEA does not have a matrix element, the solute-solute binding energy cannot be evaluated under a real local HEA lattice environment due to its complexity. Therefore, we must select matrix element, and evaluate the solute-solute binding energy based on a relative clean local environment. In this case, Ni is selected as the matrix element, because pure Ni also has a FCC lattice structure. As shown in Figure 3.19, the reference atom in maroon is fixed in a Ni supercell with the consideration of periodic boundary condition.

A second atom is placed at various nearest neighbor positions, so that the solute-solute binding energy can be evaluated by following the equation shown below:

$$E(X\text{-}Y)=E(498Ni+X+Y)-E(499Ni+X)-E(499Ni+Y)+E(500Ni) \quad (3.01)$$

where X and Y are representing two solute atoms, E( ) represents the potential energy of the corresponding system ( ).

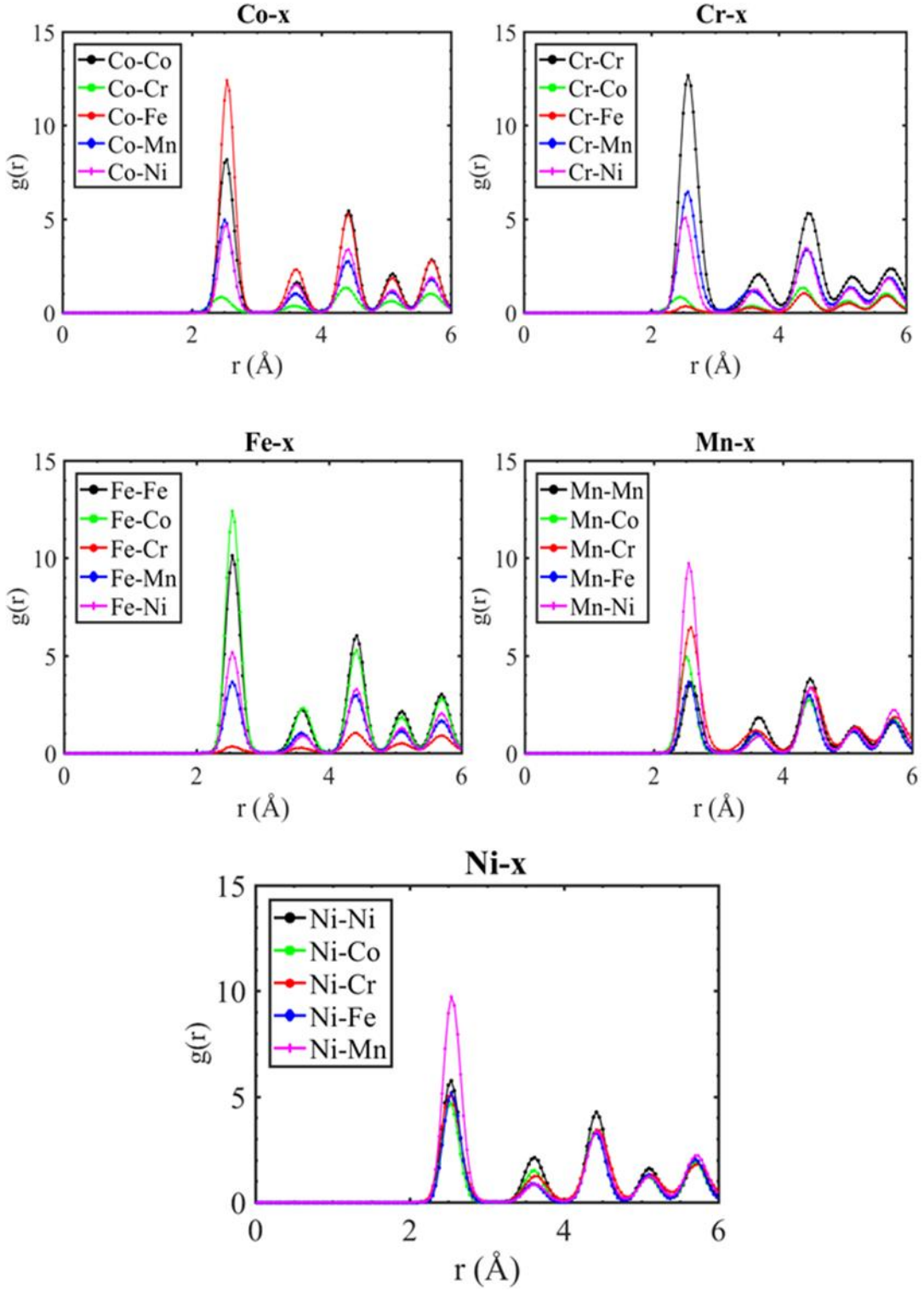

Figure 3. 18 RDF profiles for Co-x, Cr-x, Fe-x, Mn-x in the HEA after MC simulations

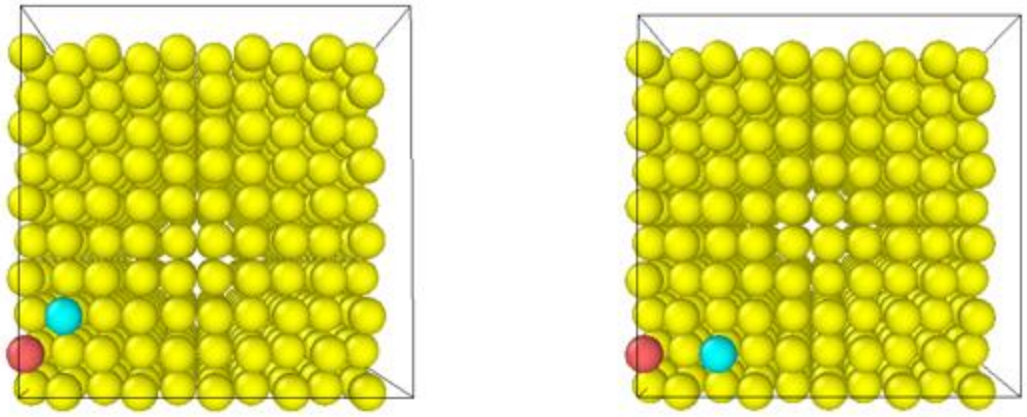

Figure 3. 19 First (left) and second (right) nearest neighbor positions (light blue) relative to the reference atom shown in maroon. Matrix Nickel atoms are shown in yellow.

a

The binding energy variation of Co-Cr, Co-Fe, Fe-Cr, Co-Mn, Cr-Mn and Ni-Mn with respect to solute-solute distance are plotted in Figure 3.20. Strong repulsive interaction are observed between Fe-Cr, Cr-Mn, Co-Cr, and Co-Mn when they are first nearest neighbors, which is consistent with RDF plots. On the other hand, strong attractive interactions are observed between Co-Fe and Ni-Mn.

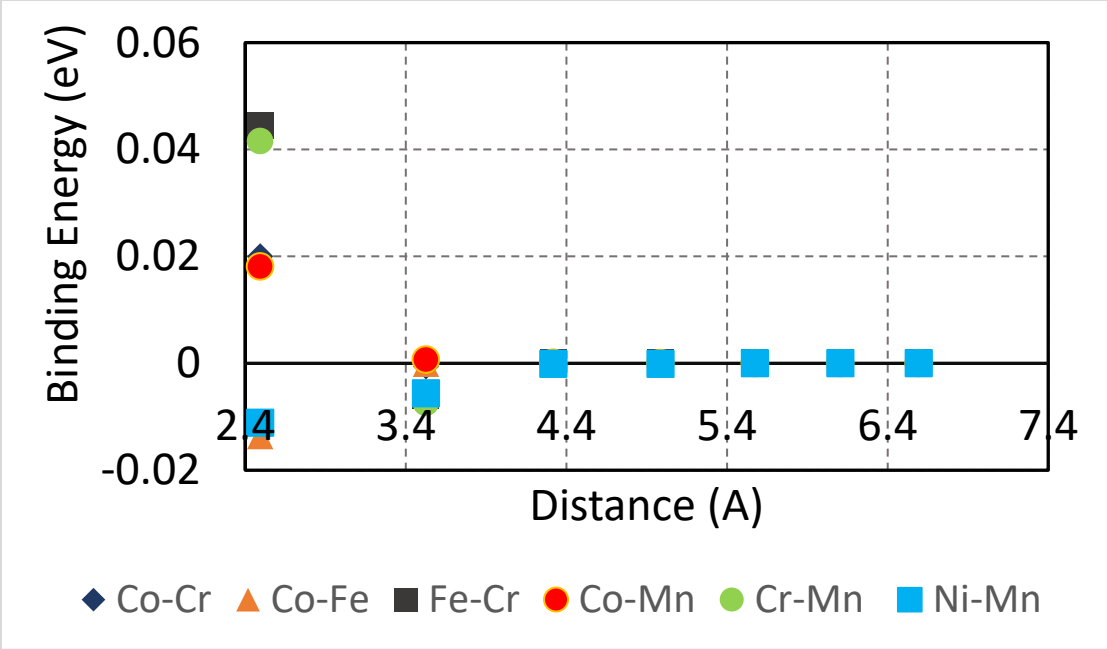

Figure 3. 20 Binding energy of atom pairs in the HEA at different neighbor positions

3.5 Chapter summary

In this chapter, we have employed MD/MC simulations to study the segregation of elements to a symmetric tilt boundary in CoCrFeMnNi. The results show that Cr has the highest tendency to occupy the grain boundary even in the presence of a free surface. Outside the grain boundary, localized clustering of Cr-Cr, Co-Fe, and Ni-Mn element pairs revealed by RDF plots. A binding energetics study confirms the attractive interactions between atom pairs which affects initially uniform element distribution in and outside the grain boundary. These results are in agreement with recent literature. Luo *et* al. studied equilibrium concentrations at an asymmetric $\Sigma 81$ GB in CrMnNi and CoCrFeMnNi at 1000K using MD/MC. In the case of the ternary alloy, weak segregation of Cr and Mn was observed, while strength co-segregation of Cr and Mn occurred in the quinary CoCrFeMnNi [122]. MD/MC simulations recently conducted by Chatain *et al.* on single

crystal CoCrFeMnNi at 1200K and their predictive analytical model shows strong Mn segregation to the surface [121]. Grain boundary atom probe tomography maps of a CoCrFeMnNi after tensile testing at 973K show stronger Cr segregation and Ni-Mn cosegregation [123].

In Chapter 4, MD/MC simulations will be used to investigate the effect of selective doped GB on tensile and compressive strength of the bi-crystal CoCrFeMnNi.

CHAPTER 4. SELECTIVE DOPING ON THE GRAIN BOUNDARY AND HEA STRENGTHENING

In this chapter, we investigate the effect of selective doping on the GB and their impact to the tensile and compressive strengths of a bi-crystal CoCrFeMnNi HEA structure. The selective doping effects on strength, stiffness, and dislocation evolution during the deformation are investigated.

4.1 Simulation Setup

We employed the ∑5 (3 1 0)[0 0 1] θ =36.9^{o} bicrystal CoCrFeMnNi HEA model in the previous study as the initial configuration for the selective doping process. Energy minimization was carried out using the conjugate gradient method with energy tolerance of 10^{-24} eV and force tolerance of 10^{-24} eV/Å. The energy minimized structure was then equilibrated at room temperature and 1atm for 0.1ns. The time step is 1fs. 800, 000 hybrid MD/MC swapping steps were then carried out under the NPT ensemble at room temperature and 1 atm. After every 10 MD steps, 10 selected doping atoms in the grain will be selected and randomly swapped with the atoms belonging to the GB with the objective of achieving a more stable energy state. As the potential energy varies with respect to the MD/MC steps shown in Figure 4.1, the potential energy is quickly converged to a stable energy state under the selective doping process. The convergence rate is much faster than that of the random swapping process presented in the previous section. Comparing with five different dopants, the CoCrFeMnNi crystal with Cr doped GB has the lowest potential energy. Such result is consistent with our observation in Chapter 3 that Cr naturally segregates to the GB to occupy the largest vacant space at the GB.

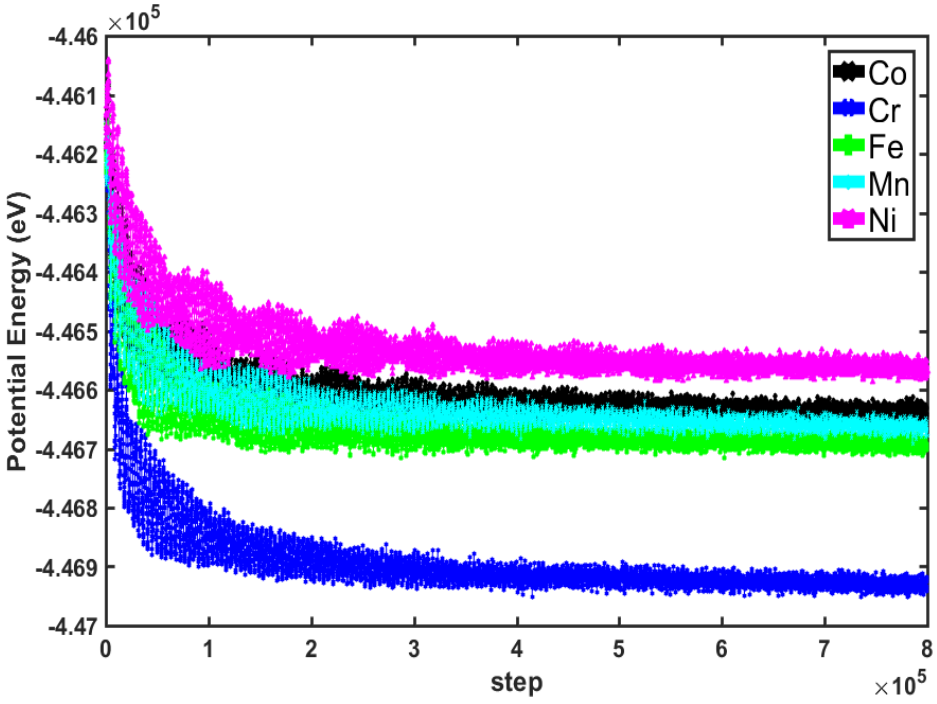

Figure 4. 1 Potential energy variation during MD/MC selective doping process

The snapshots of the bi-crystal crystal structure after the MD/MC swapping process are shown in Figure 4.2. Periodic images have been included along the longitudinal direction to fully reveal the two grain boundaries. The selected doping element present a high concentration at the GB for all the cases. All five elements remain randomly distributed within the grain.

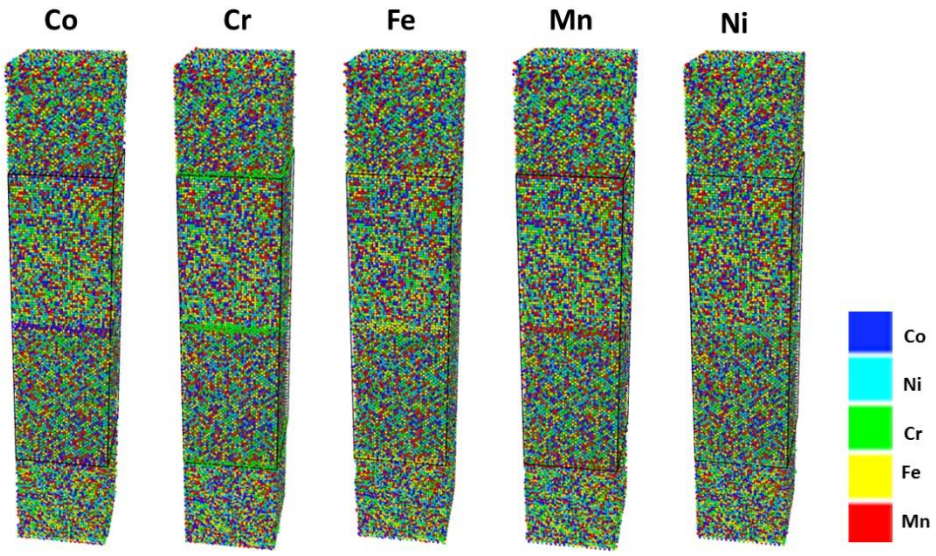

Figure 4. 2 Snapshots of bi-crystal supercell with different grain boundary dopants after selective doping. Atoms are colored based on atom type.

Consecutive *y-z* planes near the GB are selected to investigate the solute distributions, shown in Figure 4.3. The GB lattice structures on the left column are colored by the solute type. The GB lattice structures on the right column are colored by the stress field. The Mn, Fe, and Co doped GB remains the original GB kite structure, filling with larger atoms at site 1 and smaller atoms at site 4. Even though Cr doped GB has the lowest energy configuration, it results in a disordered grain boundary that does not contain the repeating kite units. The local stress distribution is also high, together with the creation of single site vacancy away from the GB.

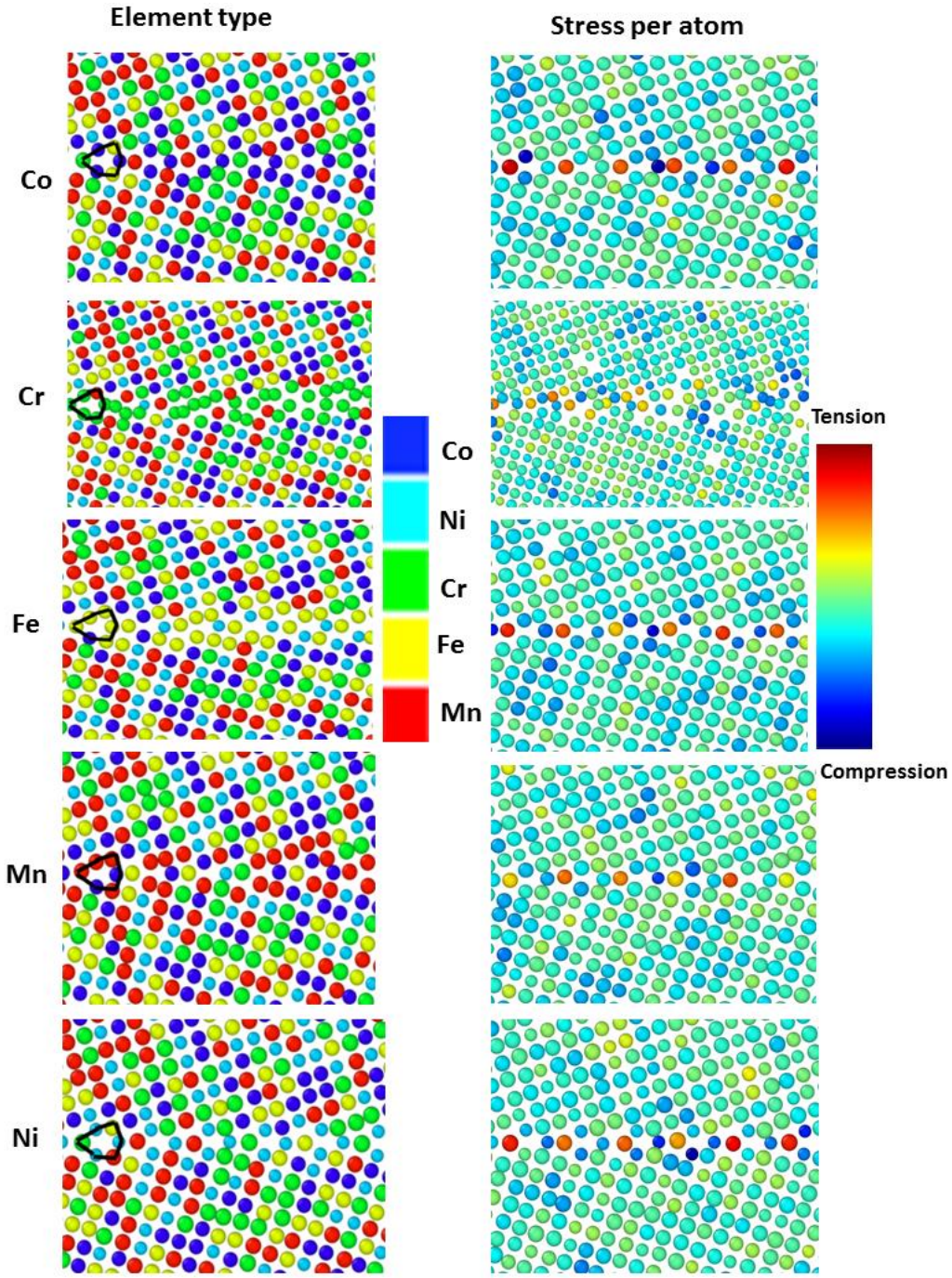

Figure 4. 3 Distribution of atoms at the grain boundary for different doping cases. The kite shape marks the repeating grain boundary units. On the left atoms are colored by type and on the right they are colored by stress per atom.

Elemental concentrations of the bi-crystal along the longitudinal direction of each selective doping case are plotted in Figure 4.4. The bin size is defined as 0.944nm along the longitudinal direction. As seen on Figure 4.4, final concentrations of each desired dopant varied based on the thermodynamics of the system, and the type of dopant affected the relative concentrations of the other four elements in different ways. Cr had the highest dopant concentration at 51% while the small atom radius Ni and Co had the lowest final concentration of 45% and 41% respectively following selective segregation.

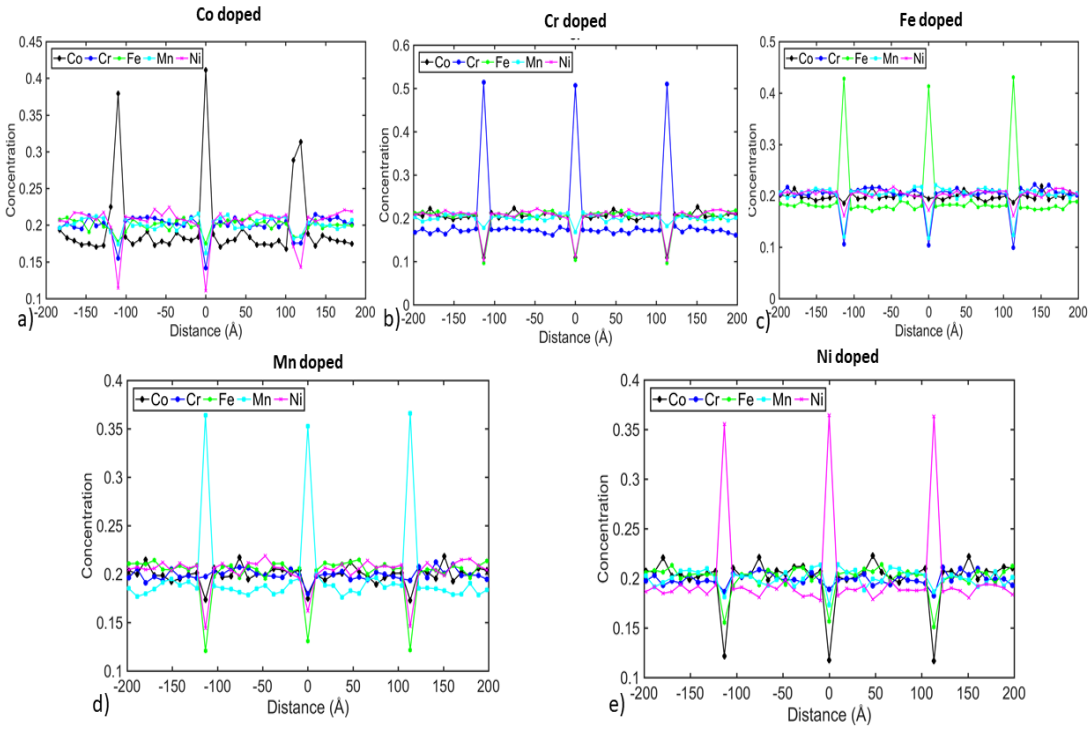

Figure 4. 4 Concentration profiles of bulk CoCrFeMnNi after selective.

4.2 Selective Dopant Effect on the Tensile Strength of Bi-crystal HEA

Before the mechanical loading tests, the structure was cooled to 77K over a period of 0.1ns and equilibrated at this temperature for another 0.1ns. In both stages, the NPT

ensemble was used, with a hydrostatic pressure of 1atm at 77K under a Nosé–Hoover thermostat and barostat. A timestep of 0.001ps was used throughout the simulation.

Tensile and compressive loads were applied along the direction which is perpendicular to the grain boundary interface. Deformation control is adopted by rescaling the simulation box length along the loading direction with a constant strain rate of 10^9 s^{-1} and rescaling the atom positions along the loading directions correspondingly. The pressure components in the lateral two directions are maintained independently at 1atm by adopting the NPT ensemble. Engineering strain components are calculated based on the current simulation box dimension and the initial simulation box dimension. Engineering stress components are determined from the pressure of the entire system of atoms.

Figure 4.5 illustrates the stress-strain relation under the uniaxial tensile test of the bi-crystal CoCrFeMnNi with selective doping on the grain boundary. A low sensitivity of Young's modulus variation w.r.t. the grain boundary selective doping can be observed from the overlapped linear elastic relation shown in the figure. Ni and Cr resulted in the highest elastic moduli of 103GPa which was a 4GPa improvement from the value of 99GPa in the random case. The experimental elastic modulus determined using resonant ultrasound spectroscopy for polycrystalline CoCrFeMnNi at 77K is 214GPa [124]. The reason for the discrepancy is the large strain rate of the MD simulation, and the structural difference between a polycrystal and bicrystal. To date, no experimental work has been published on

a bicrystal CoCrFeMnNi. The ultimate strength, however, is strongly influenced by the presence of dopants at the grain boundary.

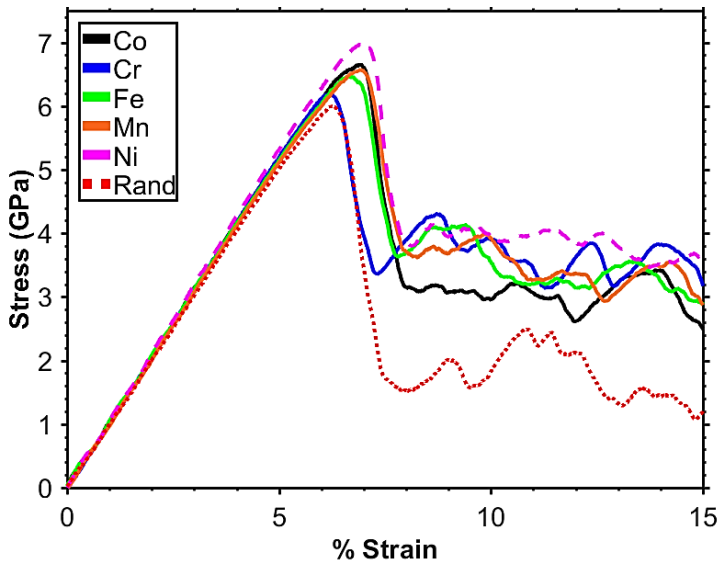

Figure 4. 5 Effects of different grain boundary dopants on the stress-strain behavior of CoCrFeMnNi under uniaxial tension

The GB with high Ni concentration results in the largest increase in the peak stress from 6.0 GPa to 7.0 GPa, and an increase in strain from 6.3% to 7.0%. Due to the naturally segregated Cr on GB, the GB with high concentration of Cr has minimum impact to the material behavior of the bi-crystal HEA under uniaxial tension. Values of ultimate strength/strain and elastic modulus are presented in Table 4.1. The elastic modulus was determined from a linear regression of the stress-strain data up to the 2% strain mark.

Table 4.1 Ultimate tensile stress and elastic modulus with selective dopped GB

Dopant	Co	Cr	Fe	Mn	Ni	Rand
Ultimate Stress (GPa)	6.7	6.2	6.5	6.6	7.0	6.0
Ultimate Strain	6.9%	6.2%	6.6%	6.9%	7.0%	6.3%
Young's Modulus (GPa)	100	103	100	101	103	99

Since grain boundaries affect dislocation movement, the presence of solutes at the GB will affect the dislocation nucleation energy barrier. The dislocation nucleation near the GB is characterized by the DXA tool and the corresponding stress required for dislocation nucleation is evaluated From Figure 4.6, it is observed that all initial dislocations are nucleated at the grain boundary. The dislocations formed at the boundary were identified as Shockley partial dislocations with Burgess vectors (1/6)[1 1 2] and (1/6)[1 1 −2] slipping on the (111) and (11-1) planes.

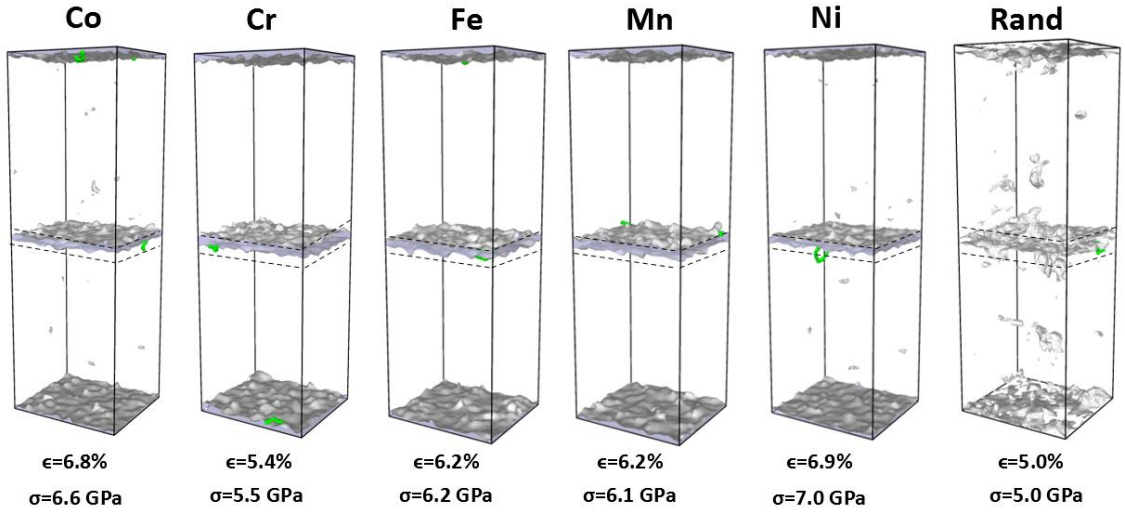

Figure 4. 6 Initial dislocation nucleation during tensile loading. All atoms have been hidden. Green lines mark the dislocation lines. GB is marked with dashed lines.

With the random GB segregation, the stress required to nucleate the first dislocation is low (5.0 GPa at a low strain of 5.0%). Among the selected doped GBs, it takes 7.0 GPa at a strain of 6.9% to nucleate the first dislocations near the GB with the highly doped Ni, and 6.6 GPa at a strain of 6.8% to nucleate the first dislocations near the GB with the highly doped Co. FCC atoms were removed to reveal the dislocation loops and slipping planes. It was also observed that dislocations slipped along the same planes in each grain in the case of the Cr dopped and random segregation HEA as shown in 4.7.

In the Fe, Co, Mn, and Ni dopped bicrystal GB, dislocations are able to cross from one grain to another causing them to change direction. In these four cases, multiple slip planes were observed in each grain. Cr has a stronger dislocation pinning effect most likely due to the severe lattice distortion or atomic mismatch caused by its large size.

Figure 4.8 shows the dislocation lines at 7.3% tensile strain. Co and the randomly dopped bicrystal GB have the lowest number of dislocations. In Figure 4.9 the evolution of dislocation density with strain is plotted. Here, the density is defined as the sum of all

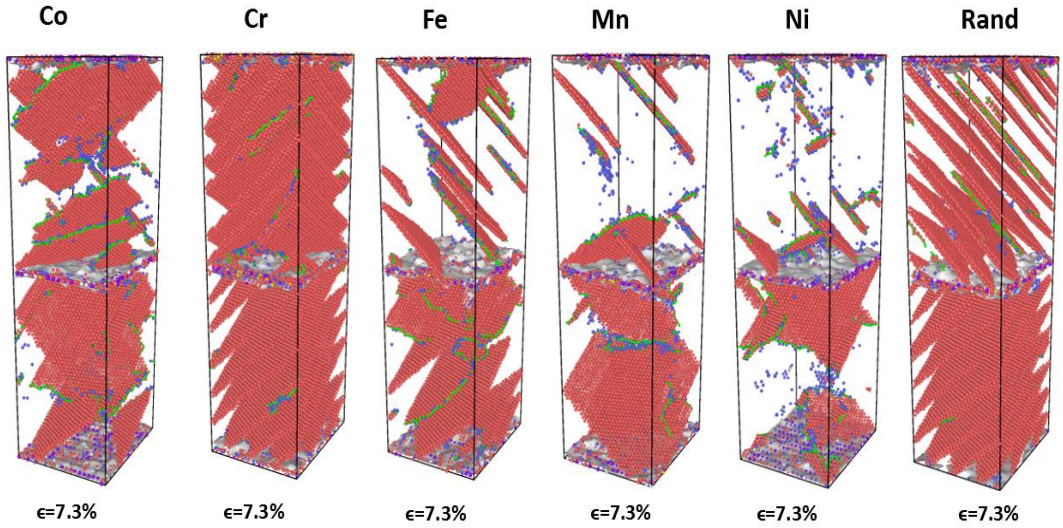

Figure 4. 7 Snapshots of dopped bicrystal under tension with different dopants. FCC atoms have been removed. Red represents HCP atom forming the stacking faults. Green line marks dislocation line. The defect mesh is shown in grey.

dislocation segments divided by simulation cell volume. A clear dependence of dislocation density on solute type is observed. Cr results in early dislocation nucleation and a shallower increase in density with strain. Ni and Co not only delay the onset of plastic deformation

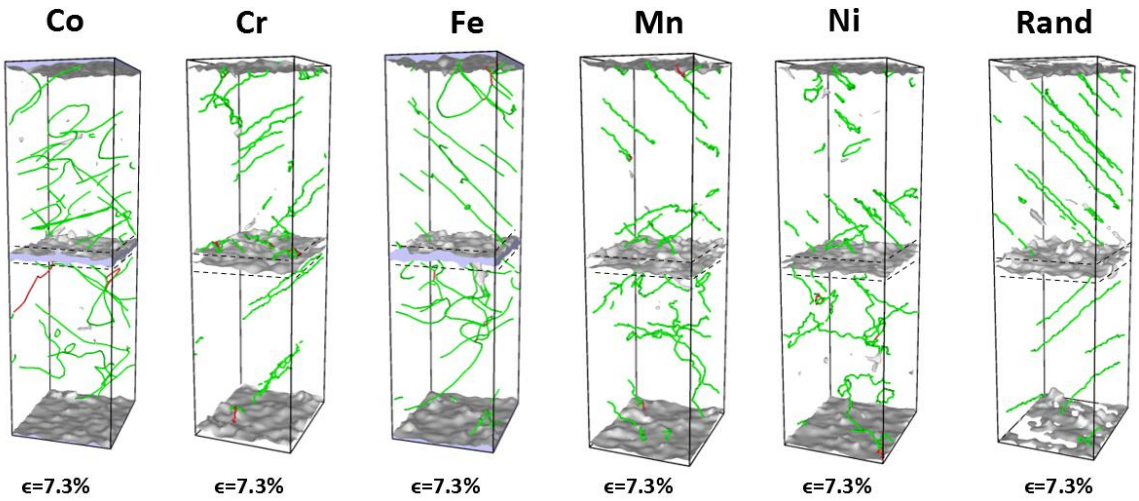

Figure 4. 8 Dislocation lines at 7.3% tensile strain. All atoms have been removed. The grey surface is the defect mesh. The green lines are dislocation lines.

but also result in a faster increase in dislocation density as seen from the slope of their respective density curves. This indicates the ease with which dislocations nucleate even during the deformation. As the stress increases, Ni results in the largest dislocation density.

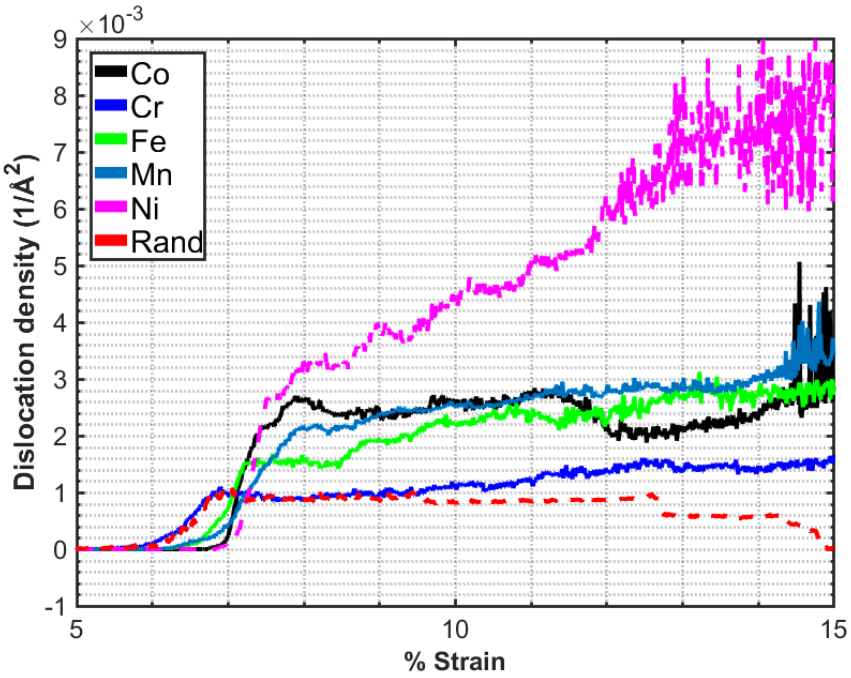

Figure 4. 9 Variation of dislocation density with respect to tensile strain .

4.3 Dopant effect on compressive strength

Uniaxial compression tests are carried out following the MD/MC process. Each bicrystal was cooled to 77K over a period of 0.1ns and equilibrated at this temperature for another 0.1ns. The NPT ensemble was used, with a hydrostatic pressure of 1atm under a Nosé–Hoover thermostat and barostat. A timestep of 0.001ps was used throughout the simulation. Compression is applied perpendicular to the GB plane through deformation control at a constant strain rate of $10^9 s^{-1}$. The pressure components in the lateral two directions are maintained independently at 1atm under NPT ensemble. The engineering stress-strain relations of the bi-crystal with various dopped GBs are shown in Figure 4.10. Cr results in the largest increase in ultimate strength from 3.6 to 4.2GPa. The ultimate strength variation with respect to different dopped GB is insignificant, within ±0.2 GPa. In both tension and compression, no significant change on Young's Modulus. Of the 5 dopants, Co results in the smallest improvement in strength contrary to the tensile loading case where Cr leads to the lowest strength improvement.

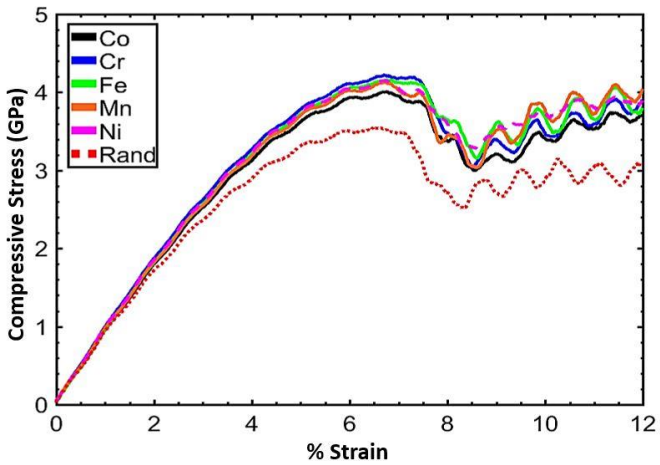

Figure 4. 10 Effects of different grain boundary dopants on the stress-strain behavior of CoCrFeMnNi under uniaxial compression

Table 4. 2 Ultimate compressive stress and elastic modulus with different dopants at GB

Dopant	Co	Cr	Fe	Mn	Ni	Rand
Ultimate Stress (GPa)	4.0	4.2	4.2	4.1	4.2	3.6
Ult. Strain	6.8%	6.7%	6.9%	6.7%	6.7%	6.5%
Young's Modulus (GPa)	89	92	89	89	91	85

Initial dislocation snapshots are shown in Figure 4.11. Like the tensile loading case, all dislocations nucleate at the grain boundary except for the random segregation case where the dislocations nucleate outside the grain boundary. Unlike in tensile loading where Ni clearly results in the highest dislocation initiation stress of 7 GPa and peak stress, Ni, and Fe have the highest dislocation nucleation stress of 4.2GPa. Consistent with the tension test, the random case has the lowest dislocation nucleation stress, Young's modulus, ultimate strength, and ultimate strain.

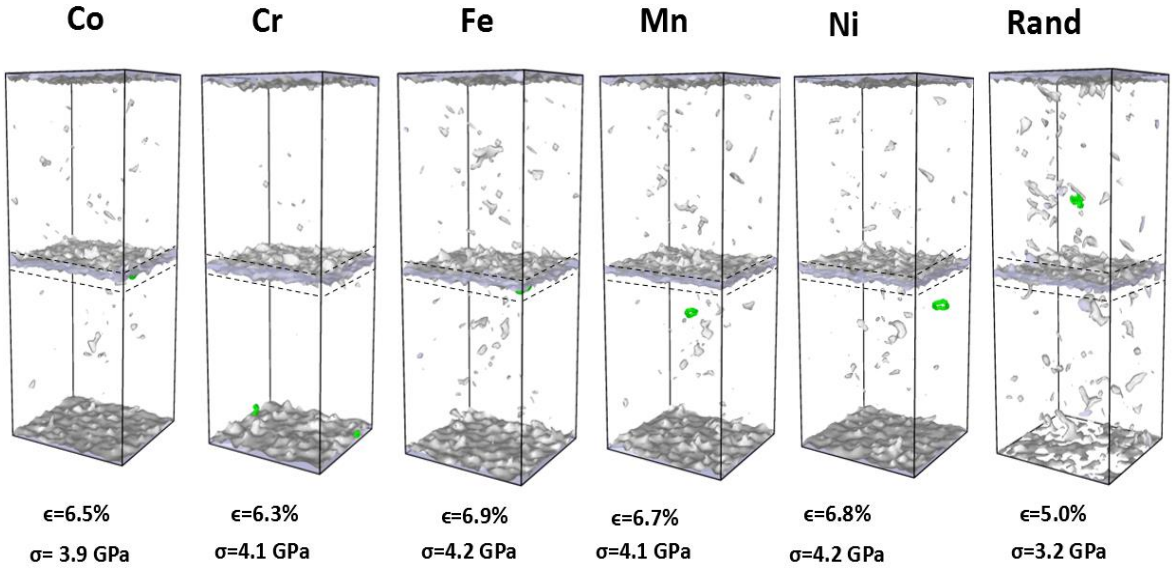

Figure 4. 11 Initial dislocation nucleation during compressive loading. All atoms have been hidden. The green lines mark the dislocation lines. The defect mesh is shown in grey.

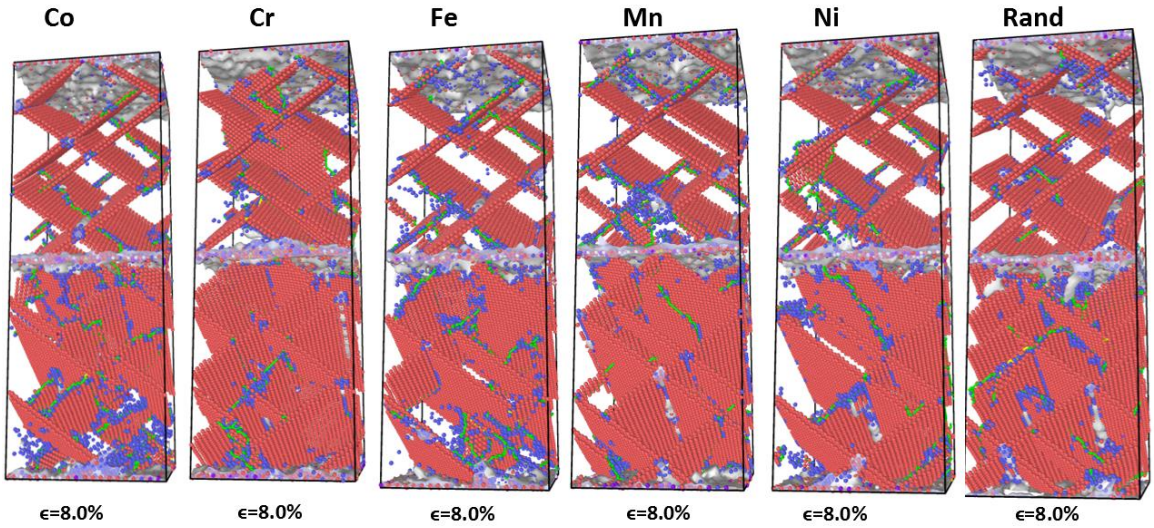

Figure 4. 12 Snapshots of dopped bicrystal under uniaxial compression at 8% strain with different dopants. FCC atoms have been removed. Red represents HCP atom forming the stacking faults. Green line marks dislocation line. The defect mesh is shown in grey.

Figure 4.12 shows the snapshots of the atomic structure with FCC atoms hidden to show the stacking faults and dislocation lines. In Figure 4.13, the atoms have been hidden to clearly show the dislocation lines. In all 6 bicrystals, multiple slip planes are visible.

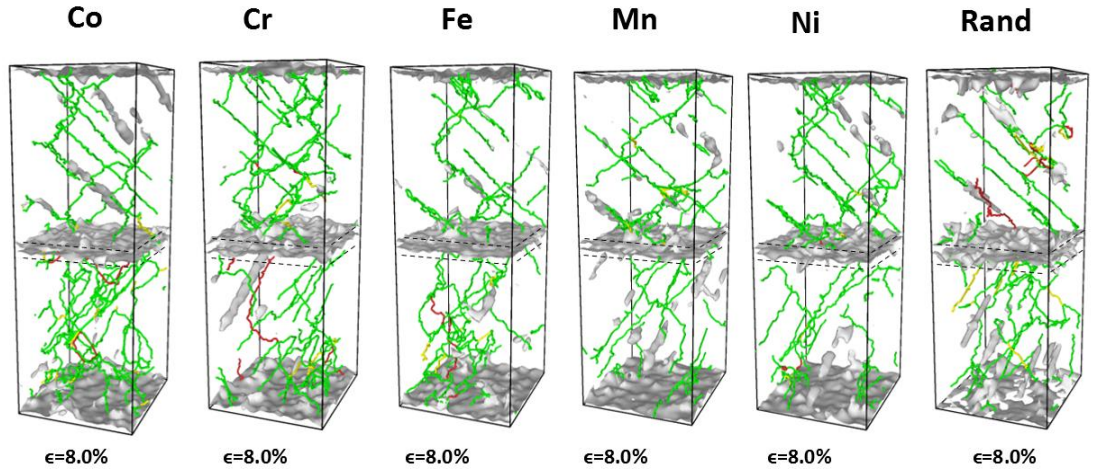

Figure 4. 13 Dislocation lines in the bicrystal under uniaxial compression at 8% strain with different dopants. All atoms been hidden for clarity.

The plot of dislocation of density versus strain in Figure 4.14 shows that at peak

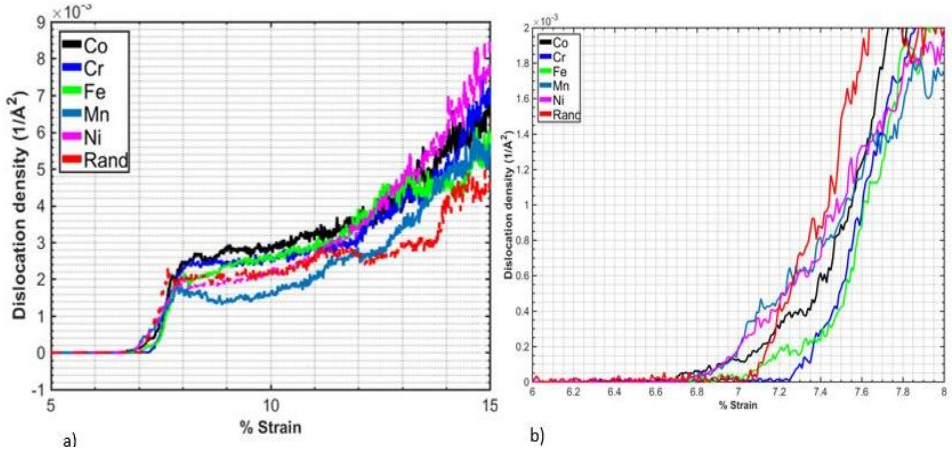

Figure 4. 14 a)Dislocation density versus strain during uniaxial compression of selectively dopped HEAs b) Close-up of dislocation plot showing dislocation initiation

stress, Mn and the random case have the highest dislocation density while Fe and Cr result in the lowest dislocation density at ultimate strength as seen in Fig, 4.14b. After the onset of plastic deformation, Cr and Fe exhibit high dislocation nucleation rates. Therefore, there is asymmetry in the deformation of the dopped HEA in tension and compression. Deformation mechanisms under compression are more complex and cannot be explained by dislocation propagation alone. In the absence of selective doped GB, the bicrystal has poor strength under uniaxial tension and compression. Ni doped GB results in good properties in both tensile and compression tests.

4.4 Chapter Summary

In this chapter, we have investigated the effects of grain boundary dopants on the strength of a CoCrFeMnNi bicrystal under uniaxial tension and compression. The randomly segregated bicrystal resulted in low ultimate strength and ductility in both tension and compression. Cr also lowered the tensile strength of the bicrystal while Ni resulted in the

tensile highest strength and ductility. No noticeable differences were observed in the ultimate compressive strength and strain of the 5 dopped bicrystals. In both tension and compression, there was no difference in Young's Modulus.

CHAPTER 5. Conclusions and Future Work

5.1 Conclusions

In this study, the segregation of each of the elements of CoCrFeMnNi to a ∑5 (3 1 0)[0 0 1] θ =36.9º grain boundary has been investigated using hybrid MD/MC simulations. This technique allowed us to efficiently obtain equilibrium elemental distributions at the GB and within the grain. Simulations revealed that Cr and Mn prefer to occupy the GB leading to the depletion of other elements. Cr had the highest concentration at the boundary of 35% and the Mn concentration was 27%. A closer look at the atom ordering at the interface revealed that Ni and Cr prefer to occupy specific sites of the repeating kite shaped boundary facets. It suggests that each unique atomic site has different segregation energy. Strong binding energy is observed between selective elements. Strong binding energy between Cr-Cr atoms leads to a high concentration of Cr at the grain boundary. Once Cr atoms are at the boundary, it was more energetically favorable to have other Cr atoms in close vicinity. Outside the grain boundary, Co and Fe atoms preferred to be close to each other due to their strong binding energy. The effect of free surfaces on elemental segregation is investigated using a nanowire model. While Cr and Fe have the lowest surface concentration of under 10%, Mn has a concentration of 45%, the concentration profile inside the HEA remained unchanged. These research findings are aligned with recent publications.

To investigate the effect of different solute concentrations at the boundary on the mechanical deformation under uniaxial tension and compression, equilibrium configurations were obtained from MD/MC simulations during which specific elements

were forced to decorate the boundary. Ni led to an increase in tensile yield and ultimate strength by increasing the dislocation nucleation stress. After yielding, more dislocations were accumulated in the Ni dopped HEA.

5.2 Future Work

This study adopts a single temperature condition and bi-crystal grain boundary condition to investigate the tensile strength tailoring of HEA through GB segregation. Further investigations can be conducted with the focus of the following aspects:

1. Other types of grain boundaries Segregation and deformation mechanisms in other symmetric/asymmetric and twist grain boundaries should be investigated. Triple junctions nanocrystalline models should be investigated.
2. Thermodynamics of segregation in quinary alloys Models can be developed to explain element segregation in multi-element materials. In addition, it is also crucial to establish how to experimentally control the elemental segregation at grain boundary.
3. Effect of temperature and loading types The behavior of GB segregation under various temperature condition and loading conditions such as cyclic loading and shear loading should be investigated. The effect of solutes on crack nucleation and propagation can be investigated.
4. Segregation of interstitial elements In addition to the substitutional segregation considered, smaller radius atoms such as Carbon and Boron can occupy interstitial sites at the grain boundary (for example, the middle of the kite

structure of the $\Sigma 5$ (3 1 0)[0 0 1] $\theta = 36.9^0$ boundary) and affect the deformation mechanisms in a different manner.

References

[1] Yeh, J.-W. et al. Nanostructured High-Entropy Alloys with Multiple Principal Elements: Novel Alloy Design Concepts and Outcomes. Advanced Engineering Materials6,299–303 (2004).

[2] Cantor, B., Chang, I., Knight, P. & Vincent, A. Microstructural development in equiatomic multicomponent alloys. Materials Science and Engineering: A375-377,213–218 (2004).

[3] Vincent, A.J.B, A study of three multicomponent alloys (BSc Part II thesis), University of Sussex, UK, 1981.

[4] Singh, S., Wanderka, N., Kiefer, K., Siemensmeyer, K. & Banhart, J. Effect of decomposition of the Cr–Fe–Co rich phase of AlCoCrCuFeNi high entropy alloy on magnetic properties. Ultramicroscopy111,619–622 (2011).

[5] Sanchez, J. M., Vicario, I., Albizuri, J., Guraya, T. & Garcia, J. C. Phase prediction, microstructure and high hardness of novel light-weight high entropy alloys. Journal of Materials Research and Technology8,795–803 (2019).

[6] Tseng, K. et al.A light-weight high-entropy alloy Al20Be20Fe10Si15Ti35. Science China Technological Sciences61,184–188 (2017).

[7] Gupta, M. & Tun, K. S. Light Weight High Entropy Alloys: Processing Challenges and Properties. Recent Patents on Materials Science10,116–121 (2018).

[8] Cayless R, Alloy and Temper Designation Systems for Aluminum and Aluminum Alloys. Properties and Selection: Nonferrous Alloys and Special-Purpose Materials15–28 (1990). doi:10.31399/asm.hb.v02.a0001058

[9] Ma, D., Grabowski, B., Körmann, F., Neugebauer, J. & Raabe, D. Ab initio thermodynamics of the CoCrFeMnNi high entropy alloy: Importance of entropy contributions beyond the configurational one. Acta Materialia100,90–97 (2015).

[10] Bracq, G. et al.The fcc solid solution stability in the Co-Cr-Fe-Mn-Ni multi-component system. Acta Materialia128,327–336 (2017).

[11] Pickering, E. J. & Jones, N. G. High-entropy alloys: a critical assessment of their founding principles and future prospects. International Materials Reviews61,183–202 (2016).

[12] El-Hadad, S., Ibrahim, M. & Mourad, M. Effect of Heat Treatment and Titanium Addition on the Microstructure and Mechanical Properties of Cast Fe31Mn28 Ni15Al24.5Tix High-Entropy Alloys. Advances in Materials Science and Engineering 2019, 1–10 (2019)

[13] Shi, Y. et al.Corrosion of Al CoCrFeNi high-entropy alloys: Al-content and potential scan-rate dependent pitting behavior. Corrosion Science 119, 33–45 (2017)

[14] Zhu, S., Du, W. B., Wang, X. M. & Han, G. F. High Mixing Entropy Alloys Design with High Anticorrosion and Wear-Resistance Properties. Advanced Materials Research815,19–24 (2013).

[15] Shi, Y., Yang, B. & Liaw, P. Corrosion-Resistant High-Entropy Alloys: A Review. Metals 7, 43 (2017)

[16] Chen, J. et al.A review on fundamental of high entropy alloys with promising high–temperature properties. Journal of Alloys and Compounds760,15–30 (2018).

[17] Wang, P., Wu, Y., Liu, J. & Wang, H. Impacts of atomic scale lattice distortion on dislocation activity in high-entropy alloys. Extreme Mechanics Letters17,38–42 (2017).

[18] Miracle, D. & Senkov, O. A critical review of high entropy alloys and related concepts. Acta Materialia122,448–511 (2017).

[19] Otto, F. et al.The influences of temperature and microstructure on the tensile properties of a CoCrFeMnNi high-entropy alloy. Acta Materialia 61,5743–5755 (2013)

[20] Ye, Y., Wang, Q., Lu, J., Liu, C. & Yang, Y. High-entropy alloy: challenges and prospects. Materials Today19,349–362 (2016).

[21] Senkov, O., Wilks, G., Scott, J. & Miracle, D. Mechanical properties of Nb25Mo25Ta25W25 and V20Nb20Mo20Ta20W20 refractory high entropy alloys. Intermetallics 19, 698–706 (2011).

[22] Senkov, O., Senkova, S., Miracle, D. & Woodward, C. Mechanical properties of low-density, refractory multi-principal element alloys of the Cr–Nb–Ti–V–Zr system. Materials Science and Engineering: A 565, 51–62 (2013).

[23] Hammond, V. H., Atwater, M. A., Darling, K. A., Nguyen, H. Q. & Kecskes, L. J. Equal-Channel Angular Extrusion of a Low-Density High-Entropy Alloy Produced by High-Energy Cryogenic Mechanical Alloying. Jom 66, 2021–2029 (2014).

[24] Yang, X., Chen, S. Y., Cotton, J. D. & Zhang, Y. Phase Stability of Low-Density, Multiprincipal Component Alloys Containing Aluminum, Magnesium, and Lithium. Jom66,2009–2020 (2014).

[25] Shao, L. et al. A Low-Cost Lightweight Entropic Alloy with High Strength. Journal of Materials Engineering and Performance 27, 6648–6656 (2018)

[26] Gorsse, S., Nguyen, M., Senkov, O. & Miracle, D. Database on the mechanical properties of high entropy alloys and complex concentrated alloys. Data in Brief21,2664–2678 (2018).

[27] Liu, W. et al.Effects of Nb additions on the microstructure and mechanical property of CoCrFeNi high-entropy alloys. Intermetallics60,1–8 (2015).

[28] Huo, W. et al.Remarkable strength of CoCrFeNi high-entropy alloy wires at cryogenic and elevated temperatures. Scripta Materialia141,125–128 (2017).

[29] Zhu, J. et al.Microstructure and compressive properties of multiprincipal component AlCoCrFeNiCx alloys. Journal of Alloys and Compounds509,3476–3480 (2011).

[30] He, J. et al.Effects of Al addition on structural evolution and tensile properties of the FeCoNiCrMn high-entropy alloy system. Acta Materialia62,105–113 (2014).

[31] Hou, J., Zhang, M., Yang, H. & Qiao, J. Deformation Behavior of Al0.25CoCrFeNi High-Entropy Alloy after Recrystallization. Metals7,111 (2017).

[32] Wu, Z., Bei, H., Pharr, G. & George, E. Temperature dependence of the mechanical properties of equiatomic solid solution alloys with face-centered cubic crystal structures. Acta Materialia81,428–441 (2014).

[33] Sun, S. et al.Enhanced strength and ductility of bulk CoCrFeMnNi high entropy alloy having fully recrystallized ultrafine-grained structure. Materials & Design133,122–127 (2017).

[34] Fazakas, É. et al.Experimental and theoretical study of Ti20Zr20Hf20Nb20X20 (X=V or Cr) refractory high-entropy alloys. International Journal of Refractory Metals and Hard Materials47,131–138 (2014).

[35] Guo, N. et al.Microstructure and mechanical properties of refractory MoNbHfZrTi high-entropy alloy. Materials & Design81,87–94 (2015).

[36] Senkov, O. N., Pilchak, A. L. & Semiatin, S. L. Effect of Cold Deformation and Annealing on the Microstructure and Tensile Properties of a HfNbTaTiZr Refractory High Entropy Alloy. Metallurgical and Materials Transactions A49,2876–2892 (2018).

[37] Yang, X., Chen, S. Y., Cotton, J. D. & Zhang, Y. Phase Stability of Low-Density, Multiprincipal Component Alloys Containing Aluminum, Magnesium, and Lithium. Jom66,2009–2020 (2014).

[38] Du, X. H., Wang, R., Chen, C., Wu, B. L. & Huang, J. Preparation of a Light-Weight MgCaAlLiCu High-Entropy Alloy. Key Engineering Materials727,132–135 (2017).

[39] Yih-Farn Kao, Ting-Jie Chen, Swe-Kai Chen, Jien-Wei Yeh, Microstructure and mechanical property of as-cast, -homogenized, and -deformed AlxCoCrFeNi ($0 \leq x \leq 2$) high-entropy alloys, Journal of Alloys and Compounds, Volume 488, Issue 1,2009, Pages 57-64

[40] Tian, L.-Y. et al.Alloying effect on the elastic properties of refractory high-entropy alloys. Materials & Design114,243–252 (2017).

[41] Huang, J.-C. Evaluation of Tribological Behavior of Al-Co-Cr-Fe-Ni High Entropy Alloy Using Molecular Dynamics Simulation. Scanning34,325–331 (2012).

[42] Zhou, X. W., Johnson, R. A. & Wadley, H. N. G. Misfit-energy-increasing dislocations in vapor-deposited CoFe/NiFe multilayers. Physical Review B69,(2004).

[43] Meraj, M. & Pal, S. Deformation of $Ni_{20}W_{20}Cu_{20}Fe_{20}Mo_{20}$ high entropy alloy for tensile followed by compressive and compressive followed by tensile loading: A molecular dynamics simulation based study. IOP Conference Series: Materials Science and Engineering 115,012019 (2016).

[44] Rao, S. et al.Atomistic simulations of dislocations in a model BCC multicomponent concentrated solid solution alloy. Acta Materialia125,311–320 (2017).

[45] Widom, M., Huhn, W. P., Maiti, S. & Steurer, W. Hybrid Monte Carlo/Molecular Dynamics Simulation of a Refractory Metal High Entropy Alloy. Metallurgical and Materials Transactions A45,196–200 (2013).

[46] Pablo, J. J. D. & Escobedo, F. A. Molecular simulations in chemical engineering: Present and future. AIChE Journal48,2716–2721 (2002).

[47] Hall, E. O. The Deformation and Ageing of Mild Steel: III Discussion of Results. Proceedings of the Physical Society. Section B64,747–753 (1951).

[48] Petch, N. J.,The Cleavage Strength of Polycrystals. Journal of the Iron and Steel Institute,174, pp. 25-28 (1953).

[49] He, W., Bhole, S. D. & Chen, D. Modeling the dependence of strength on grain sizes in nanocrystalline materials. Science and Technology of Advanced Materials9,015003 (2008).

[50] Weertman, J. Hall-Petch strengthening in nanocrystalline metals. Materials Science and Engineering: A166,161–167 (1993).

[51] Hodgson, P., Hickson, M. & Gibbs, R. Ultrafine ferrite in low carbon steel. Scripta Materialia40,1179–1184 (1999).

[52] Fang, D. et al.Effect of equal channel angular pressing on tensile properties and fracture modes of casting Al–Cu alloys. Materials Science and Engineering: A426,305–313 (2006).

[53] Suryanarayana, C. Mechanical alloying and milling. Progress in Materials Science 46,1–184 (2001).

[54] Hanna, W. et al.Nanocrystalline 6061 Al Powder Fabricated by Cryogenic Milling and Consolidated via High Frequency Induction Heat Sintering. Advances in Materials Science and Engineering2014,1–9 (2014).

[55] Erb, V. Electrodeposited Nanocrystals: Synthesis, Structure, Properties and Future Applications. Canadian Metallurgical Quarterly34,275–280 (1995).

[56] Chen, H., Jie, J.-C., Fu, Y., Ma, H.-J. & Li, T.-J. Grain refinement of pure aluminum by direct current pulsed magnetic field and inoculation. Transactions of Nonferrous Metals Society of China24,1295–1300 (2014).

[57] Nieman, G., Weertman, J. & Siegel, R. Microhardness of nanocrystalline palladium and copper produced by inert-gas condensation. Scripta Metallurgica23,2013–2018 (1989).

[58] Babicheva, R. I. et al.Effect of grain boundary segregation on the deformation mechanisms and mechanical properties of nanocrystalline binary aluminum alloys. Computational Materials Science117,445–454 (2016).

[59] Liu, X.-Y., Zhang, H. & Cheng, X.-L. Effect of nickel segregation on CuΣ9 grain boundary undergone shear deformations. Chinese Physics B27,063103 (2018).

[60] Borovikov, V., Mendelev, M. I. & King, A. H. Effects of solutes on dislocation nucleation from grain boundaries. International Journal of Plasticity90, 146–155 (2017).

[61] Zhou, X., Yu, X.-X., Kaub, T., Martens, R. L. & Thompson, G. B. Grain Boundary Specific Segregation in Nanocrystalline Fe(Cr). Scientific Reports6,(2016).

[62] Liu, X.-Y. & Adams, J. Grain-boundary segregation in Al–10%Mg alloys at hot working temperatures. Acta Materialia46,3467–3476 (1998).

[63] Bean, J. J. & Mckenna, K. P. Origin of differences in the excess volume of copper and nickel grain boundaries. Acta Materialia110,246–257 (2016).

[64] Wolf, D. Correlation between energy and volume expansion for grain boundaries in FCC metals. Scripta Metallurgica23,1913–1918 (1989).

[65] Tomozawa, M., Miyahara, Y. & Kako, K. Solute segregation on Σ3 and random grain boundaries in type 316L stainless steel. Materials Science and Engineering: A578,167–173 (2013).

[66] Dong, Y., Motta, A. T. & Marquis, E. A. Atom probe tomography study of alloying element distributions in Zr alloys and their oxides. Journal of Nuclear Materials442,270–281 (2013).

[67] Liu, B. et al.Effect of cold working and annealing on microstructure and properties of powder metallurgy high entropy alloy. Science China Technological Sciences61,197–203 (2017).

[68] Sun, S. et al.Enhanced strength and ductility of bulk CoCrFeMnNi high entropy alloy having fully recrystallized ultrafine-grained structure. Materials & Design133,122–127 (2017).

[69] Luo, H., Li, Z. & Raabe, D. Hydrogen enhances strength and ductility of an equiatomic high-entropy alloy. Scientific Reports7,(2017).

[70] Li, Z. Interstitial equiatomic CoCrFeMnNi high-entropy alloys: carbon content, microstructure, and compositional homogeneity effects on deformation behavior. Acta Materialia164,400–412 (2019).

[71] Moravcik, I. et al.Nitrogen Interstitial Alloying of CoCrFeMnNi High Entropy Alloy through Reactive Powder Milling. Entropy21,363 (2019).

[72] He, J. et al.Effects of Al addition on structural evolution and tensile properties of the FeCoNiCrMn high-entropy alloy system. Acta Materialia62,105–113 (2014)

[73] Stepanov, N. et al.Effect of V content on microstructure and mechanical properties of the CoCrFeMnNiVx high entropy alloys. Journal of Alloys and Compounds628,170–185 (2015).

[74]Qin, G. et al.CoCrFeMnNi high-entropy alloys reinforced with Laves phase by adding Nb and Ti elements. Journal of Materials Research34,1011–1020 (2019)

[75] Qin, G. et al.Strengthening FCC-CoCrFeMnNi high entropy alloys by Mo addition. Journal of Materials Science & Technology35,578–583 (2019)

[76] Thurston, K. V. et al.Effect of temperature on the fatigue-crack growth behavior of the high-entropy alloy CrMnFeCoNi. Intermetallics 88,65–72 (2017)

[77] Kontis, P. et al. Atomic-scale grain boundary engineering to overcome hot-cracking in additively-manufactured superalloys. Acta Materialia 177, 209–221 (2019)

[78] Lemarchand, D., Cadel, E., Chambreland, S. & Blavette, D. Investigation of grain-boundary structure-segregation relationship in an N18 nickel-based superalloy. Philosophical Magazine A 82, 1651–1669 (2002).

[79] L.-dong Xia, H. Chen, Z.-gang Yang, C. Zhang, Experimental and theoretical analysis of equilibrium segregation and radiation-induced segregation of Cr at grain boundaries in a reduced activation ferritic/martensitic (RAFM) steel. Journal of Iron and Steel Research International (2020), doi:10.1007/s42243-020-00484-z.

[80] E. Bolli et al., XPS study of Cr segregation in a martensitic stainless steel. Surface and Interface Analysis. 52, 1089–1092 (2020), doi:10.1002/sia.6776.

[81] L. V. Saraf, A. S. Lea, C. M. Wang, A. Dohnalkova, B. W. Arey, Chromium Segregation at the Grain Boundaries in Ni-Fe-Cr Alloys. Microscopy and Microanalysis. 16, 690–691 (2010), doi:10.1017/s1431927610056643.

[82] H. Chen, Q. Fang, K. Zhou, Y. Liu, J. Li, Unraveling atomic-scale crystallization and microstructural evolution of a selective laser melted FeCrNi medium-entropy alloy. CrystEngComm (2020) (available at https://pubs.rsc.org/en/content/articlelanding/2020/ce/d0ce00358a/unauth#!

[83] Zhang, Z. et al.A novel approach to fabricating a nanotwinned surface on a ternary nickel alloy. Materials & Design106,313–320 (2016).

[84] Vaidya, M., Guruvidyathri, K. & Murty, B. Phase formation and thermal stability of CoCrFeNi and CoCrFeMnNi equiatomic high entropy alloys. Journal of Alloys and Compounds774,856–864 (2019).

[85] Tschopp, M. A., Coleman, S. P. & Mcdowell, D. L. Symmetric and asymmetric tilt grain boundary structure and energy in Cu and Al (and transferability to other fcc metals). Integrating Materials and Manufacturing Innovation 4, (2015)

[86] Daw, M. S. & Baskes, M. I. Embedded-atom method: Derivation and application to impurities, surfaces, and other defects in metals. Physical Review B29,6443–6453 (1984).

[87] Baskes, M. I. Modified embedded-atom potentials for cubic materials and impurities. Physical Review B 46, 2727–2742 (1992).

[88] Chistyakova, N. & Tran, T. M. H. A study of the applicability of different types of interatomic potentials to compute elastic properties of metals with molecular dynamics methods. (2016). doi:10.1063/1.4964599

[89] Metropolis, N. & Ulam, S. The Monte Carlo Method. Journal of the American Statistical Association 44, 335 (1949)

[90] Metropolis, N. The beginning of the Monte Carlo method, Los Alamos Sci., 15, 125–130 (1987)

[91] Patriarca, L., Ojha, A., Sehitoglu, H. & Chumlyakov, Y. Slip nucleation in single crystal FeNiCoCrMn high entropy alloy. Scripta Materialia112,54–57 (2016).

[92] Jorgensen, W. L. & Tirado-Rives, J. Monte Carlo vs Molecular Dynamics for Conformational Sampling. The Journal of Physical Chemistry100,14508–14513 (1996).

[93] Theodorou, D. N. Progress and Outlook in Monte Carlo Simulations. Industrial & Engineering Chemistry Research49,3047–3058 (2010)

[94] Dubbeldam, D., Torres-Knoop, A. & Walton, K. S. On the inner workings of Monte Carlo codes. Molecular Simulation39,1253–1292 (2013).

[95] Zhigilei, L. Monte Carlo. Available at: http://people.virginia.edu/~lz2n/mse627/notes/MC.pdf. (Accessed: 12th July 2019)

[96] Luo, T. & Lloyd, J. R. Grand Canonical Monte Carlo Simulation of Hydrogen Adsorption In Different Carbon Nanostructures. International Journal of Energy for a Clean Environment 10, 37–56 (2009)

[97] Ji-Yuan, G. & Chang-Ming, X. Grand Canonical Ensemble Monte Carlo Simulation of Depletion Interactions in Colloidal Suspensions. Chinese Physics Letters 25, 314–316 (2008)

[98] Barr, S. A. & Panagiotopoulos, A. Z. Grand-canonical Monte Carlo method for Donnan equilibria. Physical Review E86, (2012)

[99] Tanguy, D. Monte Carlo Methodology for Grand Canonical Simulations of Vacancies at Crystalline Defects. Applications of Monte Carlo Method in Science and Engineering (2011). doi:10.5772/15838

[100] Panagiotopoulos, A. Z. Direct determination of phase coexistence properties of fluids by Monte Carlo simulation in a new ensemble. Molecular Physics 100, 237–246 (2002)

[101] Frenkel, D. Advanced Monte Carlo Techniques. Computer Simulation in Chemical Physics 93–152 (1993). doi:10.1007/978-94-011-1679-4_4

[102] Neyts, E. C. & Bogaerts, A. Combining molecular dynamics with Monte Carlo simulations: implementations and applications. Theoretical Chemistry Accounts132,(2012).

[103] Kukol, A. Molecular modeling of proteins. (Humana Press, 2008).

[104] Bonny, G., Castin, N. & Terentyev, D. Interatomic potential for studying ageing under irradiation in stainless steels: the FeNiCr model alloy. Modelling and Simulation in Materials Science and Engineering21,085004 (2013)

[105] Zhou, X. W., Foster, M. E. & Sills, R. B. An Fe-Ni-Cr embedded atom method potential for austenitic and ferritic systems. Journal of Computational Chemistry39,2420–2431 (2018)

[106] Xie, L., Brault, P., Thomann, A.-L. & Bauchire, J.-M. AlCoCrCuFeNi high entropy alloy cluster growth and annealing on silicon: A classical molecular dynamics simulation study. Applied Surface Science285,810–816 (2013).

[107] Diao, H. Y., Feng, R., Dahmen, K. A., & Liaw, P. K. (2017). Fundamental deformation behavior in high-entropy alloys: An overview. Current Opinion in Solid State and Materials Science, 21(5), 252-266. DOI: 10.1016/j.cossms.2017.08.003

[108] Woei-Ren Wang, Wei-Lin Wang, Jien-Wei Yeh, Phases, microstructure and mechanical properties of AlxCoCrFeNi high-entropy alloys at elevated temperatures, Journal of Alloys and Compounds, Volume 589,2014, Pages 143-152,

[109] Li, J., Fang, Q., Liu, B., Liu, Y. & Liu, Y. Mechanical behaviors of AlCrFeCuNi high-entropy alloys under uniaxial tension via molecular dynamics simulation. RSC Advances6,76409–76419 (2016)

[110] Liu, J. et al.Excellent ductility and serration feature of metastable CoCrFeNi high-entropy alloy at extremely low temperatures. Science China Materials62,853–863 (2018).

[111] Choi, W.-M., Jo, Y. H., Sohn, S. S., Lee, S. & Lee, B.-J. Understanding the physical metallurgy of the CoCrFeMnNi high-entropy alloy: an atomistic simulation study. npj Computational Materials4,(2018).

[112] Hou, J., Li, Q., Wu, C. & Zheng, L. Atomic Simulations of Grain Structures and Deformation Behaviors in Nanocrystalline CoCrFeNiMn High-Entropy Alloy. Materials12,1010 (2019).

[113] Do, H.-S. & Lee, B.-J. Origin of radiation resistance in multi-principal element alloys. Scientific Reports8,(2018).

[114] Bhattacharjee, P. et al. Microstructure and texture evolution during annealing of equiatomic CoCrFeMnNi high-entropy alloy. Journal of Alloys and Compounds 587, 544–552 (2014).

[115] Honeycutt, J. D. & Andersen, H. C. Molecular dynamics study of melting and freezing of small Lennard-Jones clusters. The Journal of Physical Chemistry91,4950–4963 (1987).

[116] Plimpton, S. Fast parallel algorithms for short-range molecular dynamics. (1993). doi:10.2172/10176421

[117] Nordlund, K. File:Molecular dynamics algorithm.png. Wikimedia Commons (2015). Available at: https://commons.wikimedia.org/w/index.php?curid=41419953. (Accessed: 14th March 2019)

[118] Stukowski, A. Visualization and analysis of atomistic simulation data with OVITO–the Open Visualization Tool. Modelling and Simulation in Materials Science and Engineering18,015012 (2009)

[119] Sha, W., Wu, X. & Keong, K. Molecular dynamics (MD) simulation of the diamond pyramid structure in electroless copper deposits. Electroless Copper and Nickel–Phosphorus Plating82–103 (2011). doi:10.1533/9780857090966.1.82

[120] Stukowski, A. & Albe, K. Extracting dislocations and non-dislocation crystal defects from atomistic simulation data. Modelling and Simulation in Materials Science and Engineering18,085001 (2010).

[121] D. Chatain, P. Wynblatt, Surface segregation in multicomponent high entropy alloys: Atomistic simulations versus a multilayer analytical model. Computational Materials Science. 187, 110101 (2021).

[122] Hu, Chongze & Luo, Jian. Deciphering Grain Boundary Properties in High-Entropy Alloys in a 5D Space: Coupled Segregation and Disordering. (2020)

[123] Ming, K., Li, L., Li, Z., Bi, X. & Wang, J. Grain boundary decohesion by nanoclustering Ni and Cr separately in CrMnFeCoNi high-entropy alloys. Science Advances 5, (2019).

[124] Haglund, A., Koehler, M., Catoor, D., George, E. & Keppens, V. Polycrystalline elastic moduli of a high-entropy alloy at cryogenic temperatures. Intermetallic 58, 62–64 (2015).

transitions in ternary alloys. Journal of Materials Science54,3975–3993 (2018).

[125] Rice, J. R. & Wang, J.-S. Embrittlement of interfaces by solute segregation. Materials Science and Engineering: A 107, 23–40 (1989).

[126] Hu, Y. & Rupert, T. J. Atomistic modeling of interfacial segregation and structural